_____

Composite Analysis of Atmospheric Bores during PECAN

Observed by Ground-Based Profiling Systems

_____

David M. Loveless

A thesis submitted in partial fulfillment of

the requirements for the degree of

MASTER OF SCIENCE

(Atmospheric and Oceanic Sciences)

at the

UNIVERSITY OF WISCONSIN-MADISON

2017

Thesis Declaration and Approval

I, David M. Loveless, declare that this thesis titled 'Composite Analysis of Atmospheric Bores during PECAN Observed by Ground-Based Profiling Systems' and the work presented in it are my own.

David M. Loveless   _____   _____

Author   Signature   Date

I hereby approve and recommend for acceptance this work in partial fulfillment of the requirements for the

degree of Master of Science:

Steven A. Ackerman   _____   _____

Committee Chair   Signature   Date

Jonathan Martin   _____   _____

Faculty Member   Signature   Date

Ankur Desai   _____   _____

Faculty Member   Signature   Date

Abstract

The Plains Elevated Convection At Night (PECAN) field project took place from 1 June to 15 July 2015 in the central Great Plains of the United States. As part of the project, a vast suite of instrumentation was deployed that including mobile Doppler radars, aircraft, and six fixed profiling sites and four mobile profiling units with high-temporal resolution thermodynamic and kinematic profiling capabilities. The campaign focused on observations of nocturnal elevated convection and phenomena thought to be mechanisms responsible for the initiation and maintenance of elevated convective initiation. Atmospheric bores were a focal point of intensive observation periods during the PECAN campaign, providing a database of numerous bore passages.

Previous observational studies focused on bores in the context of a single case study, which are typically extraordinary examples. Atmospheric Emitted Radiance Interferometer (AERI) thermodynamic profiling at eight of the ten profiling platforms, combined with the numerous bore passages observed during the PECAN campaign, allows for a unique opportunity to combine multiple bore observations onto a uniform time and height grid. This composite analysis is created using the observations of bore passages to document changes to the boundary layer, with relevance to the convective initiation problem. This study combines all bores, not only extraordinary cases, into a single analysis to determine typical characteristics of bore passages.

The composite reveals a bore like structure, surface pressure jump, lower-tropospheric cooling along with an updraft at the time of the bore, which gives confidence to the methodology. Maximum composite mean quasi-permanent parcel displacements are on

the order of 700 m, similar to observations in previous case studies. Time series of composite mean convective indices are calculated. Convective Inhibition (CIN) and the Level of Free Convection (LFC) is shown to decrease with the bore passage, while Convective Available Potential Energy (CAPE) is shown to decrease. Results suggest that bores increase the potential for convective initiation in the post-bore environment, but may cause convection to be less intense than if convection occurred in a pre-bore environment.

Acknowledgements

Being able to be get out in the field on a project like PECAN was amazing and I am so grateful to everyone at SSEC for giving me the opportunity to have that experience. To everyone who I got to enjoy being out in the field with, thank you for those moments, there are memories that I will keep with me forever.

To Nadia, thank you for getting me spun up on the PECAN project and for helping me to get acclimated to this new graduate school environment. To Tim, for all the discussion and guidance and patience with me throughout this project. To Steve, for academic advising and additional discussion on this project. To Ankur and Jon for their comments to help improve this project.

To all my Oneonta friends, thank you for your support and encouragement, even though we are hundreds to thousands of miles apart now. To Alex, Kate, Keiko, and Luke for all those moments of our first year when we didn't think we would make it but we still managed to push each other through. To my officemates (past and present), thank you for making it so much fun to come to school/work (I still don't know what to call it) every day.

To Skylar for ensuring there was never a dull moment in the last 2 years. To Michelle, thank you for our walks together, for our meals together, for always supporting me, for being someone I could walk with and grow in my faith with, and for being my best friend. Lastly to my family, I cannot thank you enough for all the support and love you have given me. I would never be writing this today without you all.

Table of Contents

List of Figures

List of Tables

I. Introduction

Convective weather accounts for up to 70% of warm season (April – September) precipitation in the central Great Plains of the United States (Fritsch et al. 1986). Many of these locations have a well-documented nocturnal maximum in convective precipitation (Wallace 1975, Heideman and Fritsch 1988, Colman 1990). Mesoscale convective systems (MCS), a large cluster of multicellular thunderstorms that produce a continuous precipitation area greater than 100 km (a commonly used definition noted by Houze 2004), are generally the primary producer of this nocturnal precipitation in the plains states (Fritsch et al. 1986, Heidman and Fritsch 1988, Houze 2004). The prominence of MCSs in producing flash floods has been shown in both Maddox et al. (1979) and Ashley and Ashley (2008). Ashley and Ashley (2008) found that MCSs were responsible for 36% of all flood fatalities in the United States from 1996 to 2005.

MCSs, and nocturnal convection in general, occur with a stable surface layer and elevated instability. Radiational cooling of the surface at night creates a stable nocturnal boundary layer. As a result, convection is elevated, or decoupled from the surface, which means that observed convection consists of rising parcels that originate above the nocturnal stable boundary layer. Because of this, traditional daytime triggers for convection, like differential diabatic heating, have limited application to the problem of elevated convection.

Several potential mechanisms exist with respect to explaining the initiation and maintenance of such elevated convective systems. Tripoli and Cotton (1989a, 1989b) suggest that gravity waves created by outflow from daytime convection in the Rocky Mountains play a role in triggering elevated convection in the Plains. Raymond and Jiang (1990) used

numerical simulations to show the development of a mid-level potential vorticity (PV) anomaly, due to modifications to the temperature profile through persistent convection. This PV anomaly would be self-sustaining by generating additional lift ahead of or downshear of the anomaly and descent behind the anomaly, thus maintaining the convection and temperature profile modification to maintain and strengthen the PV anomaly. The nocturnal low-level jet (LLJ) is also important in transporting high equivalent potential temperature (θ_e) air from the Gulf of Mexico region into the MCS region in the Plains (Pu and Dickinson 2014). Tuttle and Davis (2006) found that MCSs are often found at the northern end of the LLJ, a region associated with low-level convergence due to the decelerating flow.

An additional mechanism is the atmospheric bore, which is a type of gravity wave that forms as a result of the interaction between a stable boundary layer and dense evaporationally cooled air from thunderstorm outflow (e.g. Rottman and Simpson 1989, Haase and Smith 1989). Model simulations of MCS-like systems by Parker (2008) suggest that atmospheric bores play an important role in maintaining convection as the instability becomes elevated. Numerous studies of individual bores (e.g. Weckwerth et al. 2004, Knupp 2006, Koch et al. 2008) have observed vertical parcel displacements of 200 m or greater as a bore passes. Many studies have also observed convective initiation associated with a bore passage (Karyampudi et al. 1995, Locatelli et al. 2002, Wilson and Roberts 2006, Koch et al. 2008, Coleman and Knupp 2011). A commonly held hypothesis is that a bore propagating ahead of the MCS will either destabilize the boundary layer or initiate convection on its own, generating new thunderstorm cells and contributing to the maintenance of the MCS (Parker 2008). The present study investigates the potential effects of bores with respect to maintenance and initiation of convection using a composite analysis of numerous bore events.

Because elevated convection is decoupled from the surface, it is difficult to observe processes occurring with respect to the initiation and maintenance of the convective activity without vertical profiles. Radiosondes provide accurate in-situ profiles of temperature and moisture above the surface; however, radiosonde stations are separated generally by more than 500 km across the Plains states, and are only launched twice per day: 2300 and 1100 UTC (for 0000 and 1200 UTC numerical weather prediction assimilation cycles, respectively). Meanwhile, in the United States, almost the entire life cycle of nocturnal convection occurs during the period between 0000 and 1200 UTC. Thus, the radiosonde network is extremely limited in capturing these proposed mechanisms for initiating and sustaining elevated nocturnal convection. The Plains Elevated Convection At Night (PECAN, Geerts et al. 2017) field campaign, which took place during the summer of 2015, deployed a wide variety of fixed and mobile observing systems to study these mechanisms. An additional theme of the PECAN campaign was to provide a testbed for a network of thermodynamic and kinematic profilers in light of the National Research Council's (NRC) report in 2009 highlighting the need for a network that provides high-temporal resolution thermodynamic and kinematic profiling of the boundary layer. A major feature of the PECAN project (to be described further in the following section) was the creation and utilization of an integrated sounding array of mobile and fixed observing platforms.

In this study, the ability of the instrumentation to observe bores will be qualitatively assessed through the investigation of multiple cases. Additionally, the potential effects of bores on destabilizing the boundary layer will be assessed in order to better understand the role they have in the initiation and maintenance of elevated convection. To evaluate how the boundary layer typically responds to bore passages, a composite analysis of bore events,

observed during the PECAN campaign, will be created. While previous studies have investigated single events (eg. Koch et al. 1991, Koch and Clark 1999, Knupp 2006, Coleman and Knupp 2011), the present study is the first to use uniform instrumentation and methodology to composite bores on a uniform time and height scale.

II. Atmospheric Bores

A gravity, or density current is the flow of a denser fluid beneath a less dense fluid as a result of the difference in density between the two fluids in a system (Simpson 1982). Thunderstorm outflow, cold pools, and sea breezes are typical gravity currents in the atmosphere, while salt water moving upriver during high tide in a coastal estuary is a typical form of a gravity current in ocean environments. Figure 2.1 displays a schematic diagram of thunderstorm outflow as an example of the flows associated with the leading edge of gravity currents. Internal bores are a type of gravity wave that form as a result of the interaction between a gravity current and a stable fluid of lesser density which results in partially blocked flow and allows the hydraulic jump, or bore, to form. In this partially blocked flow, the gravity current is the object "blocking" the flow of the stable less dense fluid. In order for the flow to be partially-blocked, the depth of the gravity current must be less than the depth of the stable fluid.

Rottman and Simpson (1989) developed much of the hydraulic theory associated with internal bores, using a laboratory experiments in a water channel to create an idealized two layer model. Using methods originally developed by Wood and Simpson (1984), their experiment consisted of towing a thin, rounded object along the bottom of the water channel to generate a bore on the surface of the fluid. In this model, the water channel is the bottom layer and represents a stable boundary layer in the atmosphere while the air is the top layer and represents air above the stable boundary layer in the atmosphere. They also performed a second set of experiments, replacing their rounded object with releases of salt water into their two-layer channel, which simulated a gravity current (see Figure 2.2). Wood and Simpson (1984) note that the character of the bore depends on the bore strength, the ratio h_1/h_0, where

h_1 is the maximum depth of the fluid (crest of the hydraulic jump), and h_0 is the depth of the

fluid before the bore passage (Rottman and Simpson 1989). In Figure 2.2, the salt water is

the gravity current and the bore is induced ahead of the gravity current. In the context of the

atmosphere, the bore would be initiated ahead of where an outflow boundary is traveling.
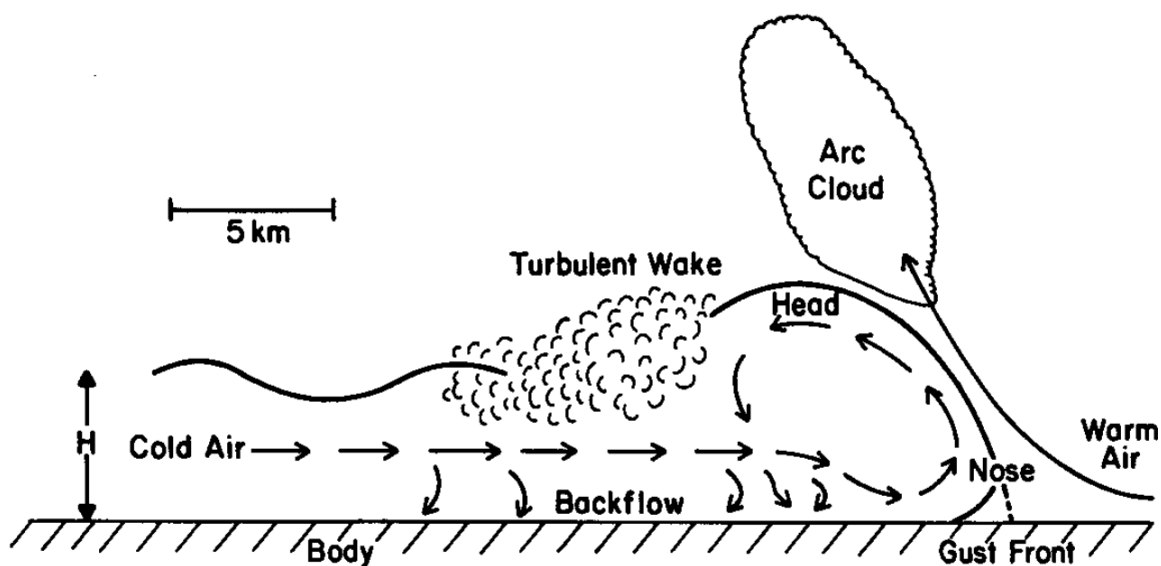
Figure 2.1: Schematic vertical cross-section of thunderstorm outflow, a type of gravity
current. (Adapted from Droegemeier and Wilhelmson 1987).
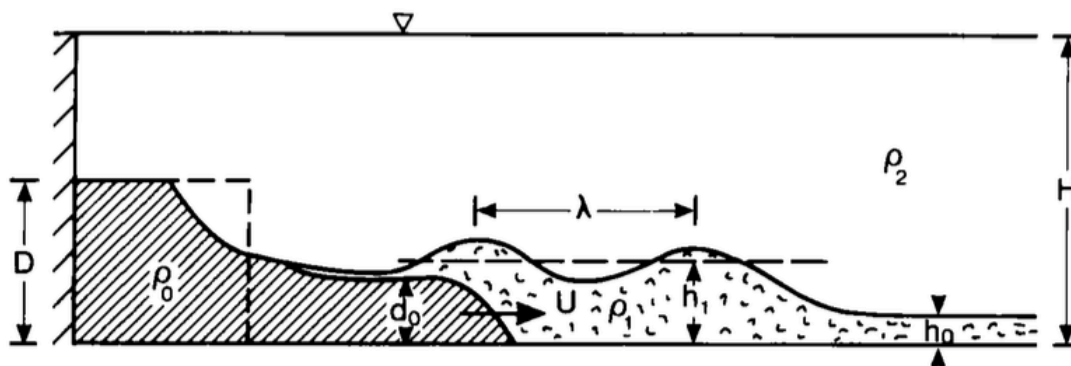
Figure 2.2: Rottman and Simpson (1989) experimental design. Gravity current (salt water) is
hatched, stable layer (freshwater) is stippled. (Adapted from Rottman and Simpson 1989).

Haase and Smith (1989) ran numerical simulations of bores and used a non-

dimensional number μ to determine if bores will form, defined as:

$$\mu = \frac{C_0}{C_{gc}} = \frac{\frac{2Nh_0}{\pi}}{C_{gc}} \qquad \text{eq. (1)}$$

where C_{gc} is the speed of the gravity current, C_0 is the long gravity wave speed $[(gh_0)^{1/2}]$, N is Brünt-Vaisala frequency at the inversion level, and h_0 is depth of the fluid prior to the bore. When μ is much less than 0.7, the gravity current is faster than the gravity waves while μ close to, but still less than 0.7 can result in undular bores that remain unseparated from the gravity current initiating them. Bores and solitary waves are formed when μ is greater than 0.7, where the gravity wave (bore or solitary wave) is faster than the gravity current. This is somewhat similar (though with gravity wave speed and Brünt-Vaisala frequency inverse to how μ is calculated) to the Froude number (Fr) used by Rottman and Simpson (1989):

$$Fr = \frac{U}{\sqrt{g'h_0}} = \frac{C_{gc}}{C_{gw}} = \frac{C_{gc}}{\sqrt{g\,d\theta\,h_0\big/\theta_{avg}}} = \frac{C_{gc}}{Nh_0} \qquad \text{eq. (2)}$$

where U is the speed of the gravity current, $d\theta$ is the change in potential temperature across the inversion, and θ_{avg} is the average potential temperature across the inversion. Note that Fr (μ) less than 1 (0.7) is "sub-critical" flow, and greater than 1 (0.7) is "super-critical" flow, and bores can form in both types of flows. Christie (1989) notes that once the bore is generated, the gravity current is no longer essential to the evolution to the bore. Crook (1988) explains that the bore will quickly dissipate if no mechanism is present to trap the vertical propagation of wave energy. Considering theory of partially blocked flows, a gravity wave is vertically trapped when the vertical wavenumber m is imaginary, or m^2 is negative, where m^2 is defined as:

$$m^2 = l^2 - k^2 \qquad \text{eq. (3)}$$

where k is the horizontal wavenumber and l^2 is the Scorer parameter:

$$l^2 = \frac{N^2}{(U-C)^2} - \frac{\delta^2 U / \delta Z^2}{(U-C)} \qquad \text{eq. (4)}$$

in which N is Brünt-Vaisala frequency, C is the speed of a gravity wave (or bore), and U is the background wind in the direction of the bore propagation. The Scorer parameter will determine the vertical trapping ability of the atmosphere. If the Scorer parameter decreases with height, the wave energy will be trapped (Crook 1988). A low-level jet moving in the opposite direction of bore propagation tends to act as a good trapping mechanism, given the $\delta^2 U / \delta Z^2$ term (Crook 1988, Koch et al. 1991, Koch and Clark 1999).

Observational evidence for the existence of atmospheric bores has been observed as early as Tepper (1950), who found that a squall line correlated with sharp increases in surface pressure on the order of 2 hPa. He claimed that these pressure jumps were evidence of a gravity wave propagating along a nocturnal temperature inversion. He proposed that this gravity wave could be caused by temporary accelerations of the cold front into a low-level stable layer, which would eventually propagate as a gravity wave downstream into the warm sector of an extra-tropical cyclone. The idea of an atmospheric bore did not seem to exist at the time of Tepper (1950), but the conditions observed and hypotheses are consistent with what are today known as bores.

Since the Tepper (1950) study, bores have frequently been observed when cold air from thunderstorm outflow interacts with a stable boundary layer (eg: Koch et al. 1991, Locatelli et al. 1998; Knupp 2006, Koch et al. 2008, Coleman and Knupp 2011). Clarke et al. (1981) identified the Morning Glory in the Gulf of Carpentaria to be a bore generated by the interaction between a sea-breeze front and a nocturnal inversion. Wakimoto et al. (1995) observed the formation of a bore as a result of a sea-breeze front colliding with an outflow

boundary. Following the Tepper (1950) hypothesis, cold fronts have also been observed to act as a gravity current and result in bore formation in the presence of a stable boundary layer (Koch et al. 1999, Hartung et al. 2010). Atmospheric bores will propagate along the temperature inversion between the surface stable layer and the weakly stratified free troposphere (Clarke et al. 1981, Koch et al. 1991, Koch et al. 1999), and will result in lifting the inversion to a quasi-permanent greater height (Koch et al. 1991, Knupp 2006).

Atmospheric bore passages result in changes to surface conditions. A bore passage will result in a surface pressure jump to a higher pressure that is sustained for a period of time and a surface wind shift into the direction from which the bore is coming (Clarke et al. 1981; Smith 1988). The increase in surface pressure is due to the increase in the depth of the surface layer caused by the bore passage. Surface temperature changes range from negligible changes (Smith 1988; Mahapatra et al. 1991) to increases in temperature as a result of adiabatic mixing of warm air at the level of the inversion down to the cooler surface (Clarke et al. 1981, Koch et al. 1991). Surface drying and cooling will happen with the arrival of the gravity current following the bore (Koch et al. 1991; Koch and Clark 1999).

The increase in the depth of the surface layer and level of the inversion results in adiabatic lifting and cooling of the lower troposphere (Koch et al. 1991, Koch et al. 2008). The magnitude of these displacements is variable, as Weckwerth et al. (2004) observed vertical parcel displacements between 500 m and 900 m with a bore passage while Knupp (2006) observed a bore that resulted in vertical parcel displacements up to 2000 m. Mechanical lifting caused by bore passage frequently results in cloud formation (eg. Clarke et al 1981, Smith et al. 1982, Knupp 2006, Coleman et al. 2010) and may trigger convective initiation if the mechanical lifting can lift parcels to their level of free convection (LFC)

(Karyampudi et al. 1995, Locatelli et al 2002, Wilson and Roberts 2006, Koch et al. 2008, Coleman and Knupp 2011). Mechanical lifting and mixing processes with bore passages have been observed to weaken the capping inversion and destabilize the boundary layer (Koch et al. 1991, Koch et al. 2008). Coleman and Knupp (2011) used temperature and moisture retrievals from a microwave profiling radiometer to make time series of convective available potential energy (CAPE) and convective inhibition (CIN) during a bore passage. They observed a decrease in surface-based CIN from 180 J kg^{-1} to 75 J kg^{-1} with a bore passage. Additionally, there was an increase in 300 m above ground level (AGL) CAPE from 75 J kg^{-1} to 300 J kg^{-1} at the time of the bore passage, which quickly decreased back to values that were observed in the pre-bore environment. Convective initiation was observed in the vicinity of this bore and soliton.

The International H$_2$O Project (IHOP_2002) took place in the southern Great Plains and while its goal was to investigate convective initiation processes in general, it provided numerous observations of bores in particular. Wilson and Roberts (2006) provided a summary of convective initiation episodes during IHOP_2002, classifying the episodes based on their trigger mechanism (fronts, outflow boundaries, drylines, pressure troughs, colliding boundaries, bores). Out of 112 episodes observed, bores triggered only three of the convective initiation episodes. While other trigger mechanisms are responsible for more frequent convective initiation (synoptic fronts and outflow boundaries were responsible for most of these episodes), individual case studies have shown the role bores can have in major initiation events. Numerical model simulations by Karyampudi et al. (1995) showed that a bore originating in the Rocky Mountains was responsible for initiating a severe squall line in western Kansas and Nebraska. Numerical simulations by Locatelli et al (2002) to study the

Super Outbreak storm from 2 – 5 April 1974 suggested that the first damaging squall line of the system (but not the one that resulted in the most tornadoes) was initiated by an undular bore. Koch and Clark (1999) showed that lifting from both a bore and gravity current resulted in initiation of a severe convective event. Model simulations of squall lines by Parker (2008) suggest that atmospheric bores play an important role in maintaining convection as the instability becomes elevated.

Rottman and Simpson (1989) found that the turbulent mixing of the bore depended on the bore strength (h_1/h_o). Turbulent processes began when bore strength was greater than 2, with much more vigorous mixing occurring with bore strength greater than 4. Mixing by bores with strength greater than 4 prevents trailing undulating solitary waves from forming, thus making the bore have the appearance of a density current (see Figure 2.1). Koch et al. (2008) used a combination of observations and numerical simulations to show that the mixing processes of bores may also be tied to the life cycle of the bore. They identified an "active phase" of the bore, during which turbulent processes are vigorous and the boundary layer and free troposphere are mixed with each other. Given a sufficiently dry free troposphere, an active phase bore can result in rapid drying of the boundary layer. Mixing processes are weaker in the "dissipation stage", which results in air being well-mixed throughout the boundary layer due to updrafts and downdrafts caused by the bore passage, but with minimal mixing between the boundary layer and free troposphere. The dissipation stage case observed by Koch et al. (2008) resulted in moistening of the boundary layer. Boundary layer rapid drying and moistening events were observed by Tanamachi et al. (2008) and concluded to be caused by bore passages.

Tepper (1950) used one-minute synoptic maps and time series of surface pressure observations at various stations to follow pressure jumps that formed ahead of a squall line. Since then, observational studies of bores have utilized radiosonde soundings (eg. Koch et al. 1991, Koch et al. 2008), photography (Coleman et al. 2010), and ground-based profiling instruments in addition to surface observations. Knupp (2006), Koch et al. (2008), and Tanamachi et al. (2008) used AERIs in their observational analysis, similar to what is used in this analysis, although these older studies used an older and less robust algorithm to retrieve the thermodynamic profiles. Tanamachi et al. (2008) concluded that water vapor profiles from instruments such as the AERI could indicate the presence of bores before they trigger convection.

Again, while atmospheric bores do not result in as frequent convective initiation as other mechanisms such as fronts or outflow boundaries, they have been shown in many studies to initiate convection, including playing a role in major severe episodes. One of the most significant, and surprising, results of the IHOP_2002 campaign was the frequent presence of bores associated with nocturnal convective events (Weckwerth et al. 2004). Additionally, their hypothesized importance to the maintenance of mesoscale convective systems (Parker 2008) suggests further study of these phenomena. This resulted in bores being one of the focal points in the Plains Elevated Convection At Night project (Geerts et al. 2017, to be described more in the next section).

Current literature on atmospheric bores has been limited to case studies of individual bores from an observational and/or modeling perspective. This presents a problem, as there is likely a selection bias that favors extraordinary cases. Additionally, there is no work that attempts to characterize to the typical changes to the boundary layer with a bore passage in a

composite sense. Furthermore, no literature that addresses the difference between bores that aid in convective initiation, and bores that do not. The present work addresses these outstanding issues by incorporating a large sample of bores, regardless of their convective initiation implications, into a single analysis to understand in general what changes a bore makes to the boundary layer, as opposed to studying a single particularly notable event.

III. Plains Elevated Convection At Night (PECAN)

The Plains Elevated Convection at Night (PECAN) campaign took place from 1 June 2015 to 15 July 2015 in the Great Plains region of the United States. Figure 3.1 displays the PECAN study region, extending from southern Nebraska to northern Oklahoma, and from Colorado to eastern Nebraska, Kansas, and Oklahoma. While this was the intended study region, observations by mobile platforms during the campaign were made as far east as Indiana and as far north as South Dakota. PECAN was designed to advance the scientific understanding and forecast skill of the processes that initiate and maintain nocturnal convection in the Great Plains. The campaign had four primary focal points: 1) initiation and early evolution of elevated convection, 2) MCS internal structure and microphysics, 3) the characterization of bores and other wave-like features, and 4) storm- and MCS-scale numerical weather prediction. The study region was selected to cover a region that included frequent low-level jet formation (pink lines in Figure 3.1 denote low-level jet frequency), mesoscale convective system (MCS) formation (MCS climatology displayed as brown dashed lines in Figure 3.1), along with frequent convective initiation and bore events.

The campaign was designed to test four overarching hypotheses, which correlate to the four science objectives. These hypotheses are: 1) Nocturnal convection is more likely to be initiated and sustained in regions of mesoscale convergence above the stable boundary layer. 2) The microphysical and dynamical processes involved in the development and maturing of nocturnal MCSs are critical to their maintenance and growth through the structure and strength of cold pools, bores, and solitary waves that interact with the stable boundary layer. 3) Bores and associated wave/solitary disturbances play a significant role in maintaining or initiating elevated nocturnal MCSs by lifting parcels above the stable

boundary layer to their level of free convection. 4) The assimilation of a mesoscale network of surface, boundary-layer and upper-level measurements into numerical weather prediction models would significantly improve the prediction of convective initiation, and produce improvements to the quantitative precipitation forecast (QPF).
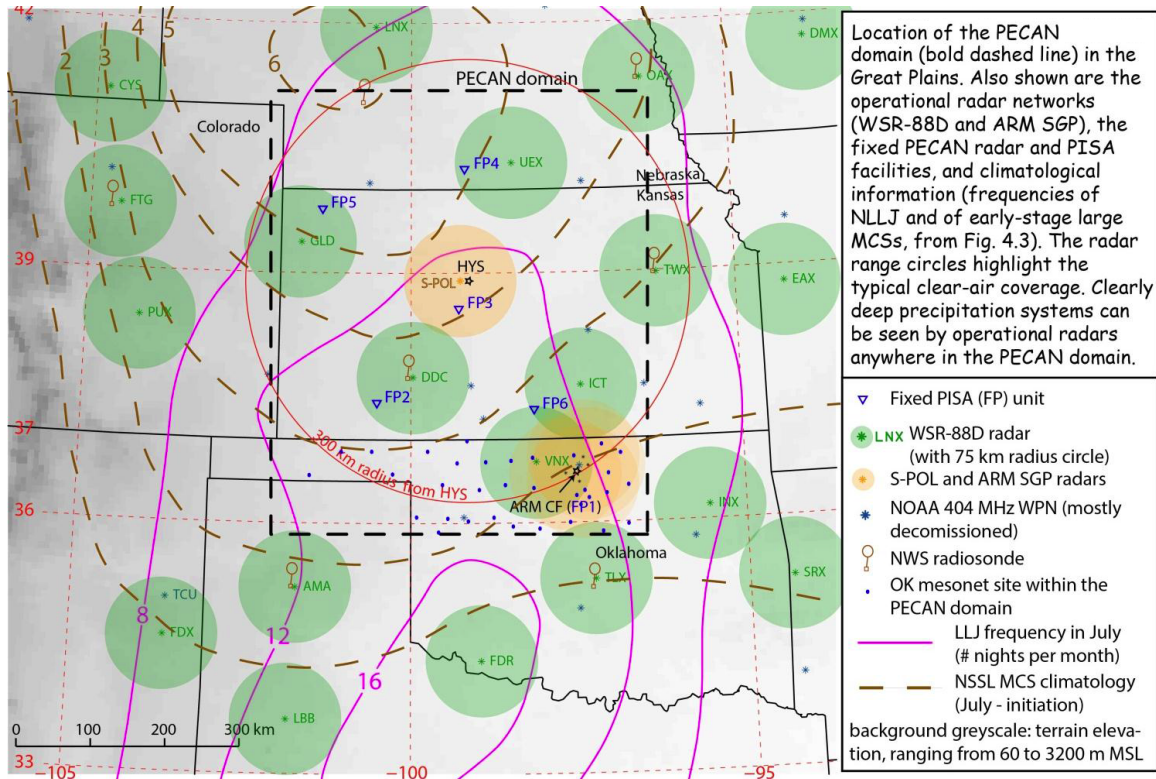
Figure 3.1: PECAN study domain, along with locations of WSR-88D radars, S-POL radar and fixed profiling (FP) sites. Figure from the PECAN Operations Plan (available at: https://www.eol.ucar.edu/node/5784).

Previous field campaigns have taken observations that have some relevance to PECAN science objectives, such as IHOP_2002 (International H$_2$O Project, Weckwerth et al. 2004), BAMEX (Bow Echo and Mesoscale Convective Vortex Experiment, Davis et al. 2004), and MPEX (Mesoscale Predictability Experiment, Weisman et al. 2015). PECAN differed from these experiments in two fundamental ways: first, it emphasized nocturnal

convection and environments; and second, it featured a much more diverse suite of instrumentation.

Data collection during PECAN came from a set of six fixed observing sites, as well observations from mobile platforms including profiling units, Doppler radars, mesonets, and aircraft. The fixed profiling sites (denoted as FP in Figure 3.1) were located throughout the study region, within 120 km of a S-band radar. While most of the fixed sites were located within that radius of an operational National Weather Service WSR-88D radar, NCAR's S-POL radar was added near Hays, KS to cover a gap in central Kansas in the WSR-88D network. The 120 km threshold for the S-band radars was determined to place each fixed profiling site within the clear air return region of one of those radars, a region where outflow boundaries, bores, solitary waves, and other non-precipitation features may be observed by the radar returns. Figure 3.2 displays an example of a radar-observed bore in northern Oklahoma where the bore is seen as what is commonly referred to as a "fine line" within the clear air return region of the radar. The mobile vehicles and aircraft allowed for local, short duration observing periods (3-12 hours) in specific regions that were forecasted to be impacted by a phenomenon related to the science objectives with little advanced notice, while fixed profiling sites took continuous observations for the entire campaign. In the early morning hours following a deployment, the mobile units would position themselves strategically to allow for rapid deployment for the next night's operations given forecasted phenomena.
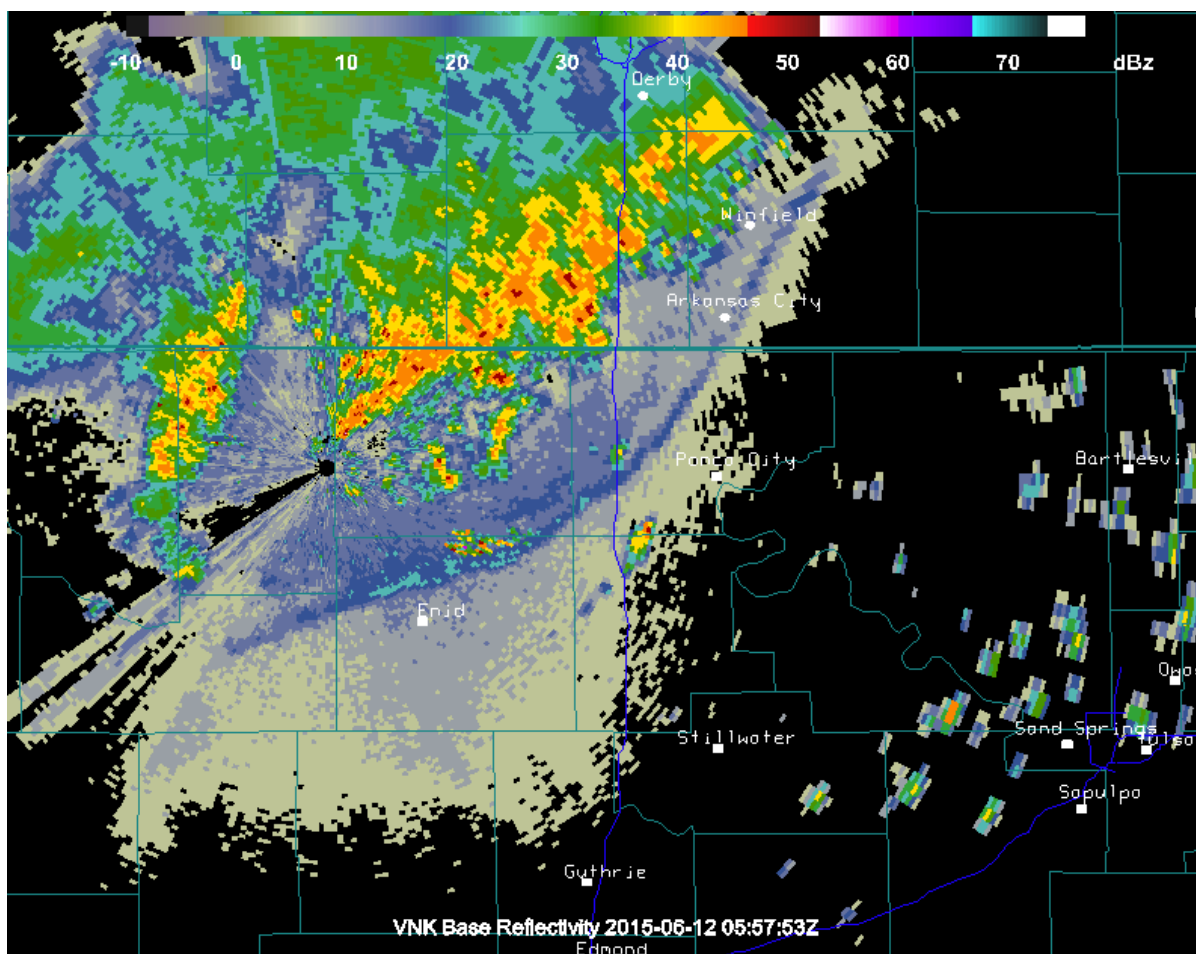
Figure 3.2: 0.5° base reflectivity observed at Vance Air Force Base, Oklahoma (VNX) at 0557 UTC on 12 June 2015. Bore is seen as what is called a "fine line" ahead of the approaching MCS.

A novel concept for PECAN compared to previous campaigns was the creation of a "PECAN Integrated Sounding Array" (PISA). The PISA consists of 10 units, the six fixed sites and four mobile profiling units, which profile the kinematic and thermodynamic structure of the lower troposphere. Each PISA facility had surface meteorology observations, radiosonde launches, and remotely sensed profiles of wind and thermodynamics, although exact instrumentation varied from one facility to the next. The instrumentation for each of the profiling units in the PISA is displayed in Table 1. The thermodynamic and kinematic

profilers provided high-temporal resolution observations of low-level temperature, moisture, and the three-dimensional wind field. This allowed for a complete observation of the evolution of the lower troposphere during the targeted weather events, which enables the assessment of the evolution of atmospheric stability (CIN, CAPE, etc.), moisture transport, mesoscale convergence, and the structure and evolution of bores and solitary waves, all at high temporal resolution. The PISA also serves as a testbed for the national network of thermodynamic profilers described in the NRC 2009 report.

Table 1: Overview of PISA thermodynamic and kinematic profiling instrumentation. Fixed PISA (FP) locations correspond with FP locations in Figure 3.1, mobile profiling units (MP) had different observing locations for each intensive observing period.

Profiling Unit	Location	Thermodynamic Profiler(s)	Kinematic Profiler(s)
FP1	Lamont, OK 36.61°N, 97.49°W	AERI MWR	Doppler lidar 915 MHz WP
FP2	Greensburg, KS 37.61°N, 99.28°W	AERI MWR	Doppler lidar
FP3	Ellis, KS 38.96°N, 99.57°W	AERI MWR Water vapor DIAL	Doppler lidar 449 MHz WP Sodar
FP4	Minden, NE 40.52°N, 98.95°W	AERI	915 MHz WP
FP5	Brewster, KS 39.38°N, 101.37°W	AERI	915 MHz WP
FP6	Hesston, KS 38.14°N, 97.44°W	AERI MWR	Doppler lidar
MP1 "CLAMPS"	N/A	AERI MWR	Doppler lidar
MP2 "MIPS"	N/A	MWR	Doppler lidar 915 MHz WP
MP3 "SPARC"	N/A	AERI	Doppler lidar
MP4 "MISS"	N/A	N/A	915 MHz WP

Mobile mesonet units were utilized during PECAN to provide additional sources of surface observations, and mobile GAUS units provided additional radiosonde measurements to supplement where the PISA did not cover. These units would frequently move during each intensive observation period in order to capture phenomena of concern as they were happening. In addition to the fixed radars (WSR-88Ds and S-POL), eight mobile radars were used with Doppler and dual-polarization capabilities to analyze storm-scale wind fields and precipitation features in both clear air and precipitating environments. The three aircraft, University of Wyoming King Air, NOAA P-3, and NASA DC-8, were used to provide additional temperature, humidity, aerosol, and wind measurements near storm environments, using a top-down approach. The mobility of the instrumentation allowed for units to be put in position to observe necessary phenomena at short notice (as science team leaders may only be certain about the forecast a few hours in advance), and to fill gaps within existing instrumentation. Additional information on PECAN experimental design, deployment strategies, and instrumentation can be found in Geerts et al (2017).

The work presented in this study utilizes observations from three fixed profiling sites (Ellis, Kansas, Minden, Nebraska, and Brewster, Kansas) and two mobile profiling units, the University of Oklahoma's/National Severe Storms Laboratory's Collaborative Lower Atmosphere Mobile Profiling System (CLAMPS), and the University of Wisconsin-Madison's Space Science and Engineering Center (SSEC) Portable Atmosphere Research Center (SPARC). These PISA units were selected because each used an Atmospheric Emitted Radiance Interferometer (AERI, Knuteson et al. 2004a, 2004b) as its thermodynamic profiling source in order to maintain uniformity in the thermodynamic observations across the different observation platforms. While this does mean that different types of wind

profilers are used (both radar and lidar profilers), this study's focus on the thermodynamic characteristics of bore passages means that the wind profiles are secondary in importance. The wind observations are interpolated to the AERI vertical and temporal observation grid. Data issues with the AERIs at FP1 (Lamont, Oklahoma), FP2 (Greensburg, Kansas) and FP6 (Hesston, Kansas) did not allow those platforms to be included in this study; while FP6 had two weeks of data available, no bore passages were recorded during that time. An overview of the instrumentation from the platforms included in this study will be given in the next section.

IV. Instrumentation

A.   Atmospheric Emitted Radiance Interferometer (AERI)

The Atmospheric Emitted Radiance Interferometer is a passive ground-based interferometer that measures downwelling atmospheric radiation at 0.5 cm^{-1} resolution from 520 cm^{-1} to 3000 cm^{-1} (19.2 μm to 3.3 μm) (Knuteson et al. 2004a, 2004b). The instrument was designed at the University of Wisconsin-Madison and then selected to be part of the Department of Energy (DOE) Atmospheric Radiation Measurement (ARM) program (Stokes and Schwartz 1994).

The instrument scans between three viewing states: two blackbodies, one at ambient air temperature and one at 60°C, are used to calibrate the system before each upward sky view. This allows the system to obtain radiometric accuracy greater than 1% of the ambient radiance (Knuteson et al. 2004b). The interferometer was originally designed to make radiance measurements across the AERI-observed spectra at a temporal resolution of 8 minutes (Knuteson et al. 2004a), but newer generations of AERIs are capable of making observations every 20 s (Turner and Löhnert 2014). An example of AERI-observed radiances is shown in Figure 4.1. From these radiances, thermodynamic profiles and trace gas concentrations may be retrieved, utilizing hyperspectral measurements around trace gas absorption bands (e.g. Smith et al. 1999, Turner and Löhnert 2014). The process of retrieving thermodynamic profiles from AERI-observed radiances is discussed in Section V. High-temporal resolution soundings provided by the AERI can observe dry lines and cold fronts (Feltz et al. 1998), monitor convective indices during severe weather events (Feltz et al. 1999, Wagner et al. 2008), and observe bore passages (Koch et al. 2008, Tanamachi et al. 2008).

AERI Observed Radiance
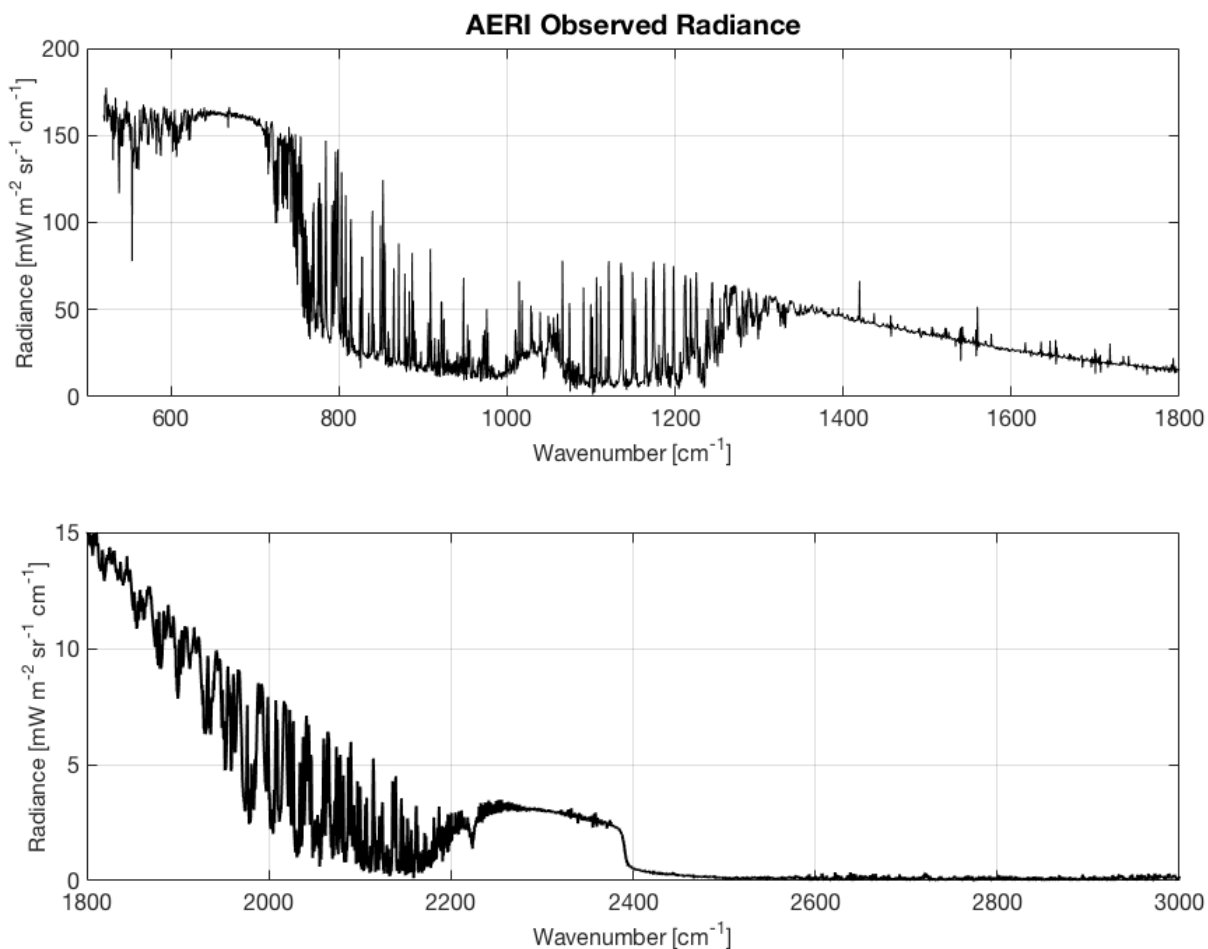
Figure 4.1: Example of AERI observed radiances with 0.5 cm^{-1} resolution observed at 2100 UTC in Hays, Kansas.

B.   Wind Profilers

Doppler lidars, 449 MHz wind profilers, and 915 MHz wind profilers provided kinematic observations of the boundary layer at the observing sites included in this study, and supplement the analysis provided by the AERI retrieved thermodynamic variables.

The Streamline Doppler lidar (HALO Photonics, Great Britain; Pearson et al. 2009) uses a 1.5 µm laser to remotely analyze wind speed and direction within the boundary layer. The lidar emits pulses at a rate of 20 kHz. Aerosols and clouds backscatter the transmitted pulses from the lidar. The along-beam component of the scatters' velocity can be computed

by considering the Doppler shift of the backscattered light. This lidar uses a Doppler beam steering method, a technique to steer the beam to point it in at least three different directions, so that both the horizontal and vertical components of the wind in the boundary layer can be computed. The depth over which the lidar can retrieve boundary layer winds is dependent on the amount of aerosols present in the boundary layer, which can be highly variable depending on both geographic location, atmospheric state, and synoptic meteorology conditions (Pearson et al. 2009). While the unambiguous range of the lidar is 7.5 km (Pearson et al. 2009), the effective range is usually limited to around 1.5 km above ground level (AGL) due to the lack of scatterers above that height. Since the optical depth of clouds at 1.5 μm is very high, a cloud base less than 1.5 km AGL reduces the effective range for kinematic retrievals. During PECAN, Doppler lidars were located with FP6, CLAMPS, and SPARC. Due to the lack of bore passages at FP6 during the periods for which AERI was active, only profiles form the latter two facilities are used in this study.

FP4 and FP5 utilized Scintec LAP-3000 915 MHz radar wind profilers to observe three-dimensional wind vector profiles. The original design of the profiler is described in Ecklund et al (1990). These radar wind profilers use a Doppler beam swinging technique to make horizontal and vertical wind measurements, detecting backscatter from inhomogeneities generated by turbulence. Data is post-processed using the NCAR Improved Moments Algorithm (NIMA, Morse et al. 2002) to enable the retrieval of winds in weak or noisy data. Its maximum unambiguous height is 5 km, but also had typical viewing heights of up to 1.5 km for the 10 minute averaged data used in this study. This is because of a combination of the reduction in signal to noise ratio, with higher temporal resolution data and a lack of turbulent generated inhomogeneities above the boundary layer.

The 449 MHz multiple antenna profile radar was used at FP3, using a 7 antenna module configuration. This system transmits and receives multiple pulses at once in different directions as opposed to using the traditional Doppler beam swinging method. Similar to the 915 MHz profiler, the 449 MHz profiler detects backscatter from temperature and humidity inhomogeneities generated by turbulence. The profiler can view up to 5 km, but the typical maximum height of observations was 3 km for the 5 minute averaged data used in this study. The phased array setup of the 449 MHz allows for better signal to noise ratio, allowing for kinematic retrievals at greater heights and greater time resolution than the 915 MHz profiler. A technical overview of the design and additional details on wind profiler performance may be found in Lindseth et al. (2012).

V.   AERIoe Retrieval Method

As discussed in the previous chapter, the AERI measures downwelling infrared radiation between 520 cm^{-1} and 3000 cm^{-1} every 20 s. To conduct noise filtering on the radiances without resorting to averaging and thus maintaining the high temporal resolution, raw spectra observations are noise filtered using a principal component analysis technique (Turner et al. 2006). Since the downwelling spectrum at the surface is a function of the state of the atmosphere above the surface, hyperspectral observations contain enough information to retrieve profiles of temperature and moisture as well as trace gas concentrations. From the filtered spectra, high-temporal resolution profiles of temperature and moisture can be retrieved using a number of physical and/or statistical approaches. This study uses thermodynamic retrievals made by an optimal estimation retrieval technique referred to as AERIoe (Turner and Löhnert 2014).

The optimal estimation approach used in the AERIoe is similar to the optimal estimation approach originally developed by Rodgers (2000). The optimal estimation equation used (equation 1 in Turner and Löhnert 2014) is as follows:

$$\mathbf{X}_{n+1} = \mathbf{X}_a + (\gamma \mathbf{S}_a^{-1} + \mathbf{K}_n^{\mathrm{T}} \mathbf{S}_e^{-1} \mathbf{K}_n)^{-1} \mathbf{K}_n^{\mathrm{T}} \mathbf{S}_e^{-1} [\mathbf{Y} - F(\mathbf{X}_n) + \mathbf{K}_n(\mathbf{X}_n - \mathbf{X}_a)] \qquad \text{eq. (5)}$$

where **K** is the Jacobian or weighting function matrix:

$$\mathbf{K}_n = \frac{\partial F(\mathbf{X}^n)}{\partial \mathbf{X}^n} \qquad\qquad \text{eq. (6)}$$

$\mathbf{X}^n$ is the current state vector at iteration n, $\mathbf{X}_a$ is the a priori, $\mathbf{Y}$ is the observation vector, F is a forward model, $\mathbf{S}_a$ is the a priori covariance matrix, and $\mathbf{S}_e$ is the observation error covariance matrix. Equation 5 differs slightly from the version derived in Rodgers (2000) in that the parameter γ, as added by Turner and Löhnert (2014), is included to change the

relative weight between the prior information and the observation. It is adjusted to smaller values with each iteration, which allows the algorithm to converge even with a poor first guess; with the addition of the γ parameter, AERIoe usually converges in approximately seven iterations.

AERIoe requires an external observation of cloud base height to calculate the liquid water path, which is necessary to produce temperature and moisture profiles in the presence of clouds. In this study, cloud base height is provided through backscatter profiles of the Doppler lidars on the mobile units (CLAMPS and SPARC), water-vapor Differential Absorption Lidar (DIAL) at FP3, and ceilometers located at or near FP4 and FP5. The ability to retrieve profiles in the presence of clouds is a notable advantage of AERIoe over the previously used AERIPROF thermodynamic retrieval algorithm (Smith et al. 1999, Turner et al. 2000, Feltz et al. 2003). Being able to retrieve profiles in cloudy sky conditions allows for more continuous profiling, with only precipitation preventing the thermodynamic retrievals, which improves the applications to weather observations.

According to the original version in Turner and Löhnert (2014), the retrieval is constrained using a first guess that is a 10-year-long radiosonde climatology from the ARM Southern Great Plains (SGP) site in Lamont, OK. The original version of AERIoe has less than 0.2 K and 0.3 g kg^{-1} mean bias in the lowest 2 km of the atmosphere in clear sky conditions compared to radiosondes at the ARM Southern Great Plains site. AERIoe also can retrieve concentrations of trace gases that absorb and emit within the AERI-observed wavelengths (eg. CO, CO_2, CH_4, etc.), but will not be utilized in this investigation.

The newest version of AERIoe, used in this study, uses profiles derived from the Rapid Refresh Model (RAP, Benjamin et al. 2016) as both a first guess and as a solution

constraint for observations above 4 km. This assumes RAP provides a better estimate of the atmosphere above 4 km than an unconstrained retrieval; as AERI information content peaks in the lower troposphere (Turner and Löhnert 2014), observed radiances contain little information about the profile above 4 km. This also improves performance of the algorithm in the lower troposphere by effectively setting the thermodynamic state of the middle and upper troposphere as known, which allows the available information content in the radiances to be applied to the near-surface atmosphere instead of to the whole atmospheric column, which increases the ability of the algorithm to retrieve atmospheric structure in the regions with greatest variability. Accuracy above 4 km is also improved, as the RAP profile is more likely to accurately represent the upper atmospheric state than radiance observations that contain little information from those levels or a climatology of radiosonde observations. Through the use of RAP profiles as first guesses and the resulting increase in accuracy of the thermodynamic observations throughout the troposphere, the retrieval of thermodynamic indices like Convective Available Potential Energy (CAPE) is improved.

Each of the FP and mobile profiling platforms with AERIs made radiosonde launches during PECAN. SPARC, FP4, FP5, and FP6 used Vaisala RS92-SGP radiosondes, FP3 used Vaisala RS41-SGP radiosondes, and CLAMPS used IMET-1 radiosondes. This provides a dataset of collocated radiosonde observations with AERI retrievals from which an evaluation study could be done for the PECAN campaign. Using radiosonde observations and AERIoe retrievals from CLAMPS, SPARC, FP3, FP4, FP5, and FP6, there were a total of 457 profile-to-profile comparisons. Of the 457 total comparisons, 252 are Vaisala RS92, 130 are Vaisala RS41, and 75 are IMET1. The AERIoe retrieval selected for the comparison was the retrieval closest in time to the average time between the radiosonde launch and the time the

radiosonde reached 4 km above ground level. The AERIoe retrieval also had to be within 15 minutes of that average time in order to be included in the comparison.

Figure 5.1 displays the root mean square error (RMSE) and bias (calculated as AERIoe retrieval minus radiosonde, thus a positive bias indicates the retrieval is warmer or more moist than the radiosonde observation) for temperature and water vapor mixing ratio. Each of the radiosondes has its own set of uncertainties, displayed in Table 2. From the RMSE, it can be determined that AERIoe is typically within 2.0 K of the radiosonde measurement in the lowest 2.0 km of the atmosphere, with near zero bias compared to the radiosonde. Above 2.0 km, a warm bias compared to the radiosonde is present in the retrievals, and RMSE increases to 2.5 K by 3.0 km above ground level. Similarly, AERIoe is generally within 1.5 g kg^{-1} of the radiosonde up to 1.5 km, also with near zero bias. Water vapor mixing ratio displays less than 1 g kg^{-1} bias compared to the radiosonde throughout the entire profile while RMSE exceeds 2 g kg^{-1} at places in the profile. These results are different than what was recorded in Turner and Löhnert (2014) because this includes all comparisons, not only clear sky profiles. This evaluation allows for the results presented in this study to be put into context given the performance of the retrieval algorithm.

Table 2: Uncertainties associated with each radiosonde type included in the AERIoe to radiosonde evaluation. Radiosonde information can be found at: International Met Systems (2006) and Vaisala (2013, 2016).

Radiosonde Type	Pressure Uncertainty	Temperature Uncertainty	Relative Humidity Uncertainty
IMET-1	0.5 hPa	0.2°C	5%
Vaisala RS41-SGP	0.4 hPa	0.3°C	5%
Vaisala RS92-SGP	1.0 hPa	0.5°C	4%
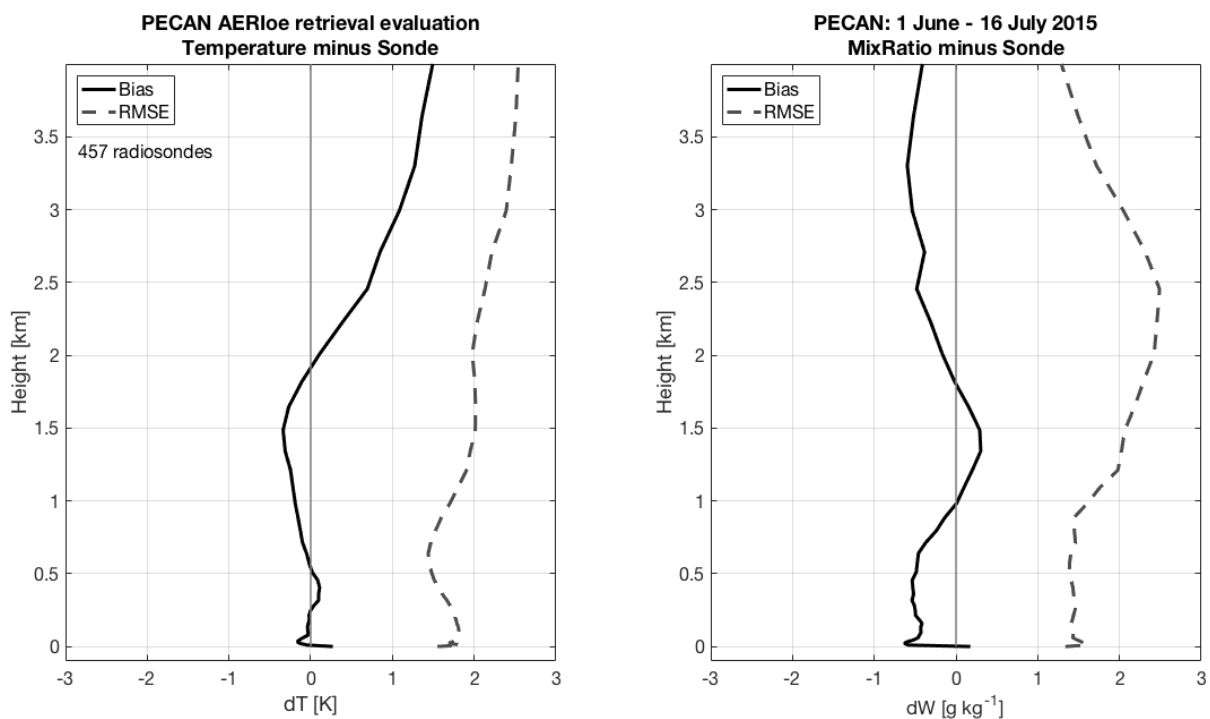
Figure 5.1: AERIoe root mean square error (RMSE) and bias (retrieval minus radiosonde) calculations for temperature (K, left) and water vapor mixing ration (g kg^{-1}, right) for the PECAN campaign, 1 June to 16 July 2015.

VI.   Evaluating AERIoe Observations of Bore Passages

As part of determining the potential applications and strengths and weaknesses of the instrumentation for a potential thermodynamic profiler network in the future, it is worthwhile to evaluate AERIoe observations of bore passages. The potential temperature retrievals from the AERIoe for a bore on 20 June 2015 at FP4 is shown in Figure 6.1. This displays the ability of the AERIoe retrievals to identify the bore front and the undulations associated with trailing solitary waves. Figure 6.2 displays the FP4 915 MHz wind profiler-observed vertical velocities for the same period of time as Figure 6.1. Similar undulations are seen in both the vertical velocity observations as the AERIoe retrievals. This shows that the AERIoe is able to resolve the undulations in the thermodynamic field at the height of about 1,000 m AGL where those solitary waves progressed. The agreement between the two observing platforms gives confidence that what the two observing platforms show are real phenomena.

The AERIoe has enough sensitivity to thermodynamic retrievals that the character of the bore may be discerned. Figure 6.3 displays a case from 26 June 2015 at FP3 in Ellis, KS in which there were no undulations occurring behind the bore. The turbulent character of the bore may also be identified with the AERIoe retrievals. This turbulence is unable to be directly observed with the 5 minute averaging time of the AERIoe retrievals and wind profiles used in this study. However, the AERIoe-retrieved water vapor retrievals may be used to discern this mixing. The rapid drying of the boundary layer during the bore passage can be observed in Figure 6.3b. This gives an indication of the mixing occurring between the moist boundary layer and the dry free troposphere. Surface observations of temperature and dew point temperature, displayed in Figure 6.4, reveal the rising temperature associated with the bore passage and the simultaneous decrease in dew point temperature associated with the

drying of the boundary layer. This is likely an "active phase" bore according to Koch et al (2008) terminology, but its type cannot be determined exactly due to the inability to calculate turbulent kinetic energy from the available instrumentation. Figure 6.5 displays the AERIoe retrievals of potential temperature and water vapor mixing ratio for a more dramatic boundary layer drying event with a bore passage from 18 June 2015. However, in this case the gravity current which follows closely behind the bore contributes to the drying, and not just the bore causing the drying on its own.
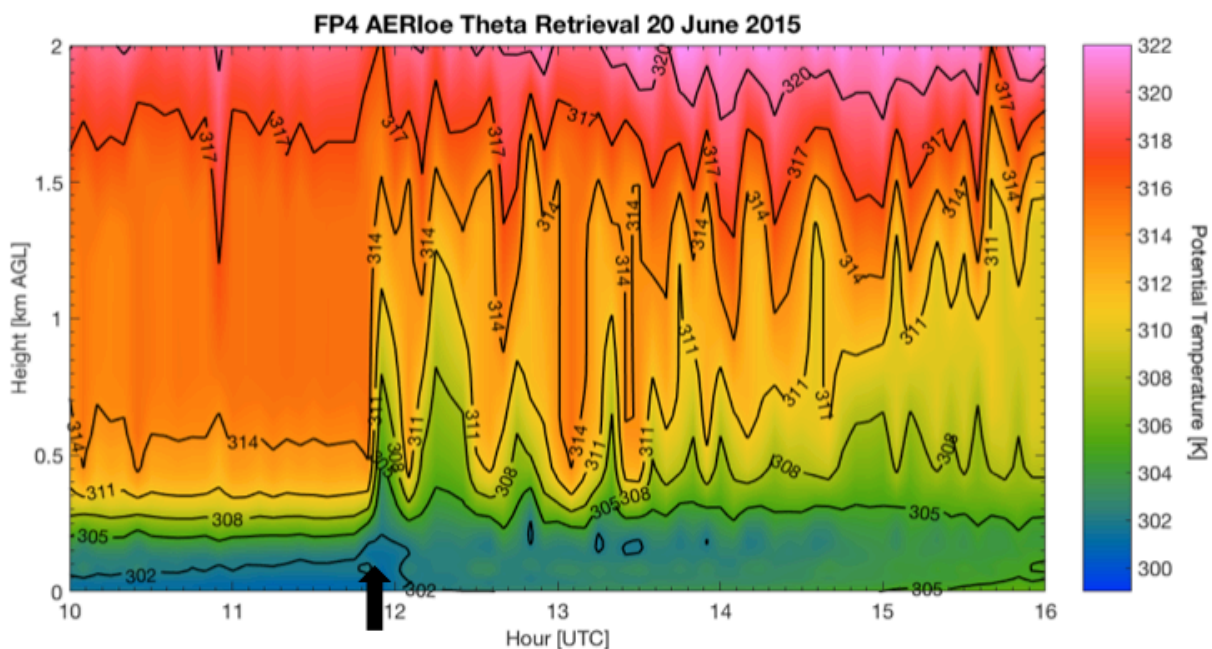
Figure 6.1: AERIoe retrieved potential temperature time-height cross-section from FP4 in Minden, NE from 20 June 2015 from 1000 UTC to 1600 UTC. Potential temperature is shaded, with isentropes outlined and labeled every 3 K. The bore start time is 1155 UTC, denoted by the black arrow.

In contrast to the 18 and 26 June 2015 cases at FP3, Figure 6.6 displays the AERIoe retrieved potential temperature and water vapor mixing ratio for 7 June 2015 at FP3. As shown in Figure 6.6a, the thermal structure of the 7 June bore appears similar to the 26 June bore (Figure 6.3a). However, Figure 6.6b displays the lofting of moisture throughout the

boundary layer, as opposed to the drying seen in the 18 and 26 June cases. The 10 g kg^{-1} isohume is lifted about 500 m in Figure 6.6b, while more elevated moisture levels, represented in Figure 6.7 by the 13 g kg^{-1} isohume disappear entirely after bore passage. Koch et al. (2008) and Tanamachi et al. (2008) both used AERI-derived thermodynamic retrievals for their observations of a drying and moistening events caused by bores in the atmosphere, but their analysis predated the development of AERIoe and instead used AERIPROF. AERIoe is able to identify bore-passage-induced changes in the boundary layer at high temporal resolution.
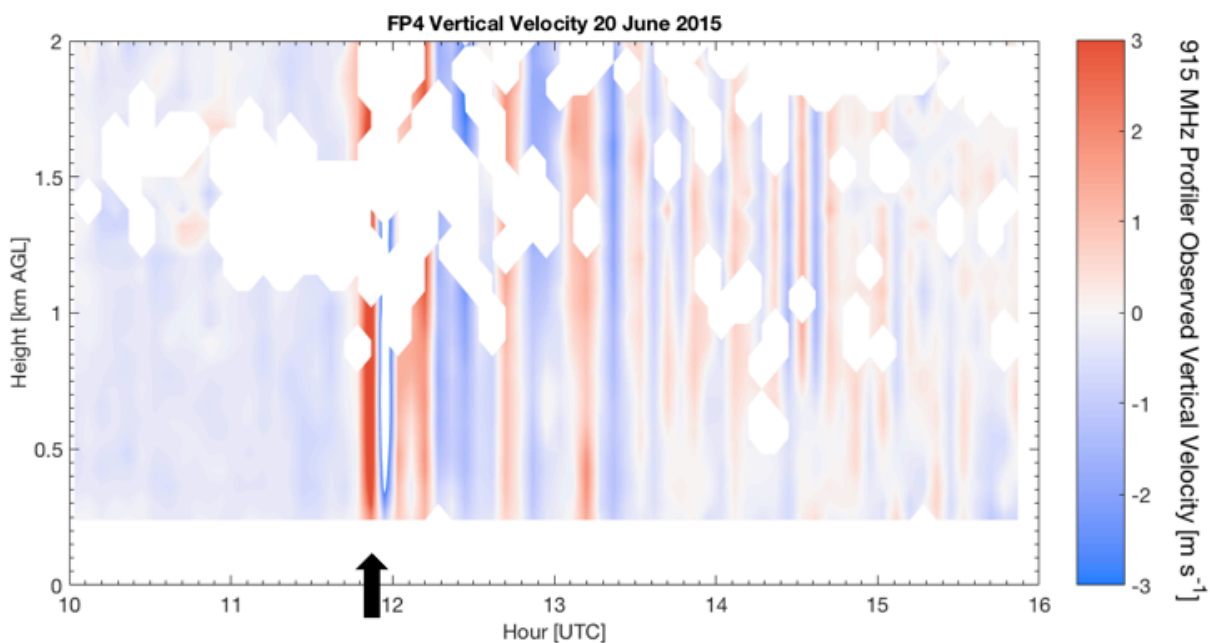
Figure 6.2: 915 MHz wind profiler retrieved 10 minute averaged vertical velocity with a 5 minute update cycle from 10 UTC to 16 UTC at FP4 on 20 June 2015. The bore start time is 1155 UTC, denoted by the black arrow.
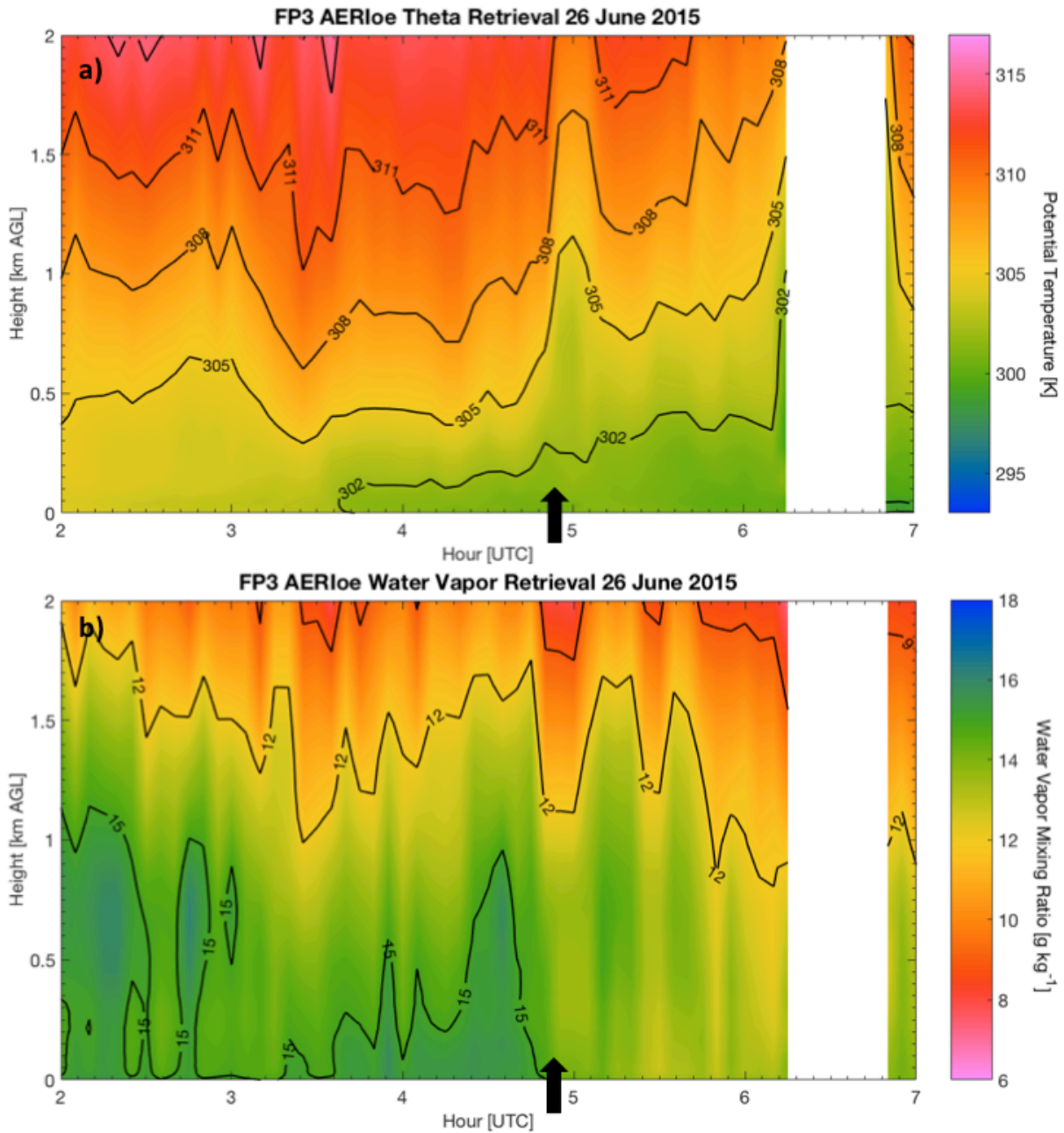
Figure 6.3: AERIoe retrieved a) potential temperature and b) water vapor mixing ratio time-height cross-section from FP3 in Ellis, KS from 26 June 2015 from 0200 UTC to 0700 UTC. Potential temperature and water vapor mixing ratio is shaded, with isentropes and isohumes outlined and labeled every 3 K and 3 g kg^{-1}. The bore start time is 0455 UTC, denoted by the black arrows. There are no retrievals between 0615 and 0650 UTC due to rain.
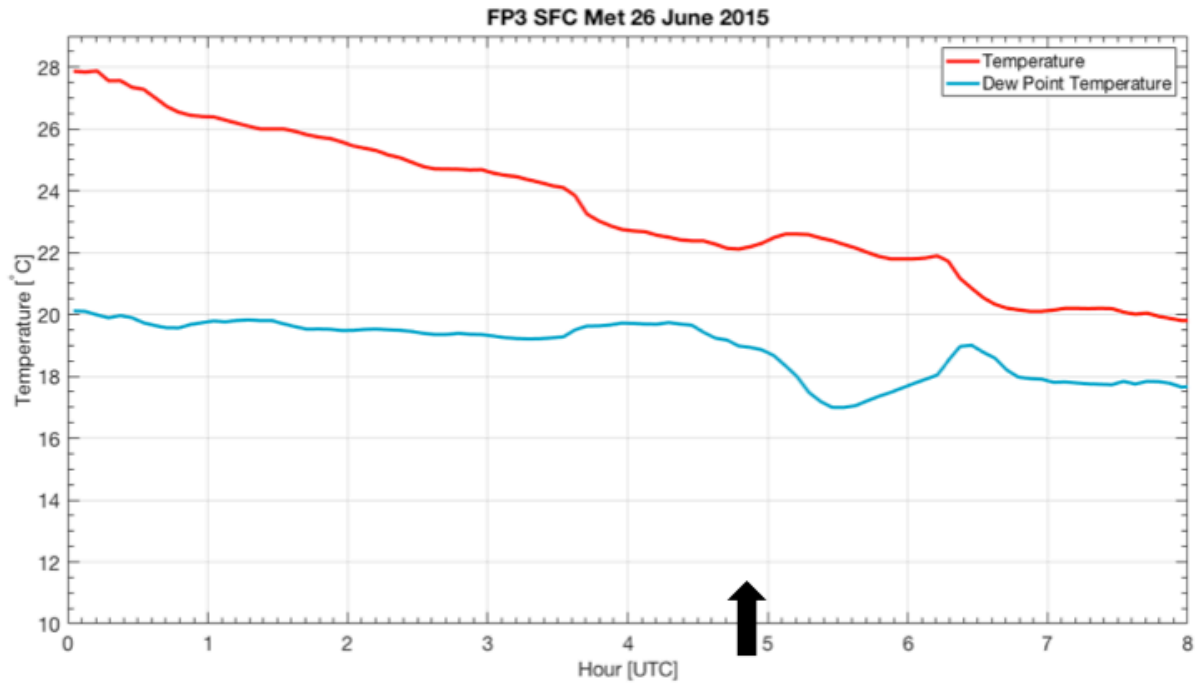
Figure 6.4: Surface temperature and dew point temperature [°C] from 00 to 08 UTC at FP3 in Ellis, KS on 26 June 2015. The bore start time is 0455 UTC, denoted by the black arrow.

Internal bore theory deals heavily with the depth of the fluid layers: the depth of the stable fluid (h_0), the depth of the gravity current (d_0), and the depth of the fluid at the peak of the hydraulic jump (h_1) are all critical for defining characteristics of the bore. In order to make comparisons of observation to theory, these parameters must be observed. Additionally, the Brünt-Vaisala frequency (N) across the inversion is needed in the calculation of the Scorer Parameter (equation 4). Radiosondes have higher vertical resolution than surface-based profilers which allows for it to resolve finer scale features, and, if launched at the correct time, would be the ideal source for identifying these parameters. However, outside of field experiments, the radiosonde network does not offer sufficient temporal density to provide both pre- and post-bore thermodynamic profiles. Even during field campaigns, pre-

and post-bore radiosonde launches are difficult to come by: only 6 of the 20 bore cases in this study have both pre- and post-bore radiosonde launches within an hour of the bore passage.

Figure 6.5: AERIoe retrieved a) potential temperature and b) water vapor mixing ratio time-height cross-section from FP3 in Ellis, KS from 18 June 2015 from 1200 UTC to 1600 UTC. Potential temperature and water vapor mixing ratio is shaded, with isentropes and isohumes outlined and labeled every 3 K and 3 g kg^{-1}. The bore start time is 1355 UTC, denoted by the black arrows.

Only thermodynamic profilers like AERI have sufficient temporal resolution to provide pre- and post-bore profiles for every bore passage over the sensor. Additionally, thermodynamic profilers provide an instantaneous retrieval of thermodynamic variables, while radiosonde observations will drift downwind horizontally, and may take tens of minutes to go vertically through the boundary layer, and 30 minutes or more to ascend through the majority of the troposphere, causing further complications to the application of the radiosonde.

One of the cases that had both pre- and post-bore radiosondes was the 26 June 2015 bore observed by SPARC. Bore passage was at 0730 UTC while SPARC operators launched radiosondes at 0707 UTC and 0752 UTC. This provides a good pair of radiosondes to which AERIoe's capabilities of identifying important bore theory parameters can be compared. Figure 6.7 displays the pre-bore radiosonde and the AERIoe retrieval at the closest time. In the pre-bore context, AERIoe identifies the correct height of the inversion. However, due to several factors, AERIoe displays a weaker inversion than identified by the radiosonde. An exponential decrease in vertical resolution due to averaging of broad weighting functions that peak at the surface (Turner and Löhnert 2014) and the smearing of the radiosonde climatology first guess result in the inability for the AERIoe to reproduce the sharp inversion observed by the radiosonde. The retrieval of a weaker inversion would decrease N compared to what would be calculated from a radiosonde profile. Figure 6.8 is the same as Figure 6.7, except for the post-bore radiosonde and AERIoe pair. The radiosonde displays the lifting of the capping inversion to a greater height (from 925 hPa to 875 hPa), but once again the AERIoe struggles to identify the inversion, due to similar reasons as explained with the pre-bore sounding. The radiosonde and AERIoe temperatures agree well at the height of the post-

bore inversion, but AERIoe is unable to sufficiently resolve enough structure at that height level to identify the post-bore inversion. There can be noise in AERIoe retrievals, with variations occurring from retrieval to retrieval that are not necessarily physical, but these problems identified in the pre- and post-bore comparisons remain the same for AERIoe retrievals +/- 10 minutes of the radiosonde time.

While the AERIoe struggles to reproduce finer scale features in the thermodynamic profiles like the inversion strength and height, the AERIoe is able to capture temporal changes in the boundary layer due to the bore passage. Quasi-permanent parcel displacements may be observed and time series of retrievals can reveal information about the turbulent mixing occurring in the bores. Observing the changes to the boundary layer caused by the bore passage are important for determining the possibility of the bore producing convective initiation. Monitoring changes to the thermodynamic field in the boundary layer allows for the ability to observe changes to the instability of the atmosphere. As will be shown in the next section, AERIoe is able to observe temporal changes in severe index calculations which allows for the changes in instability and potential for convective initiation to be quantified.
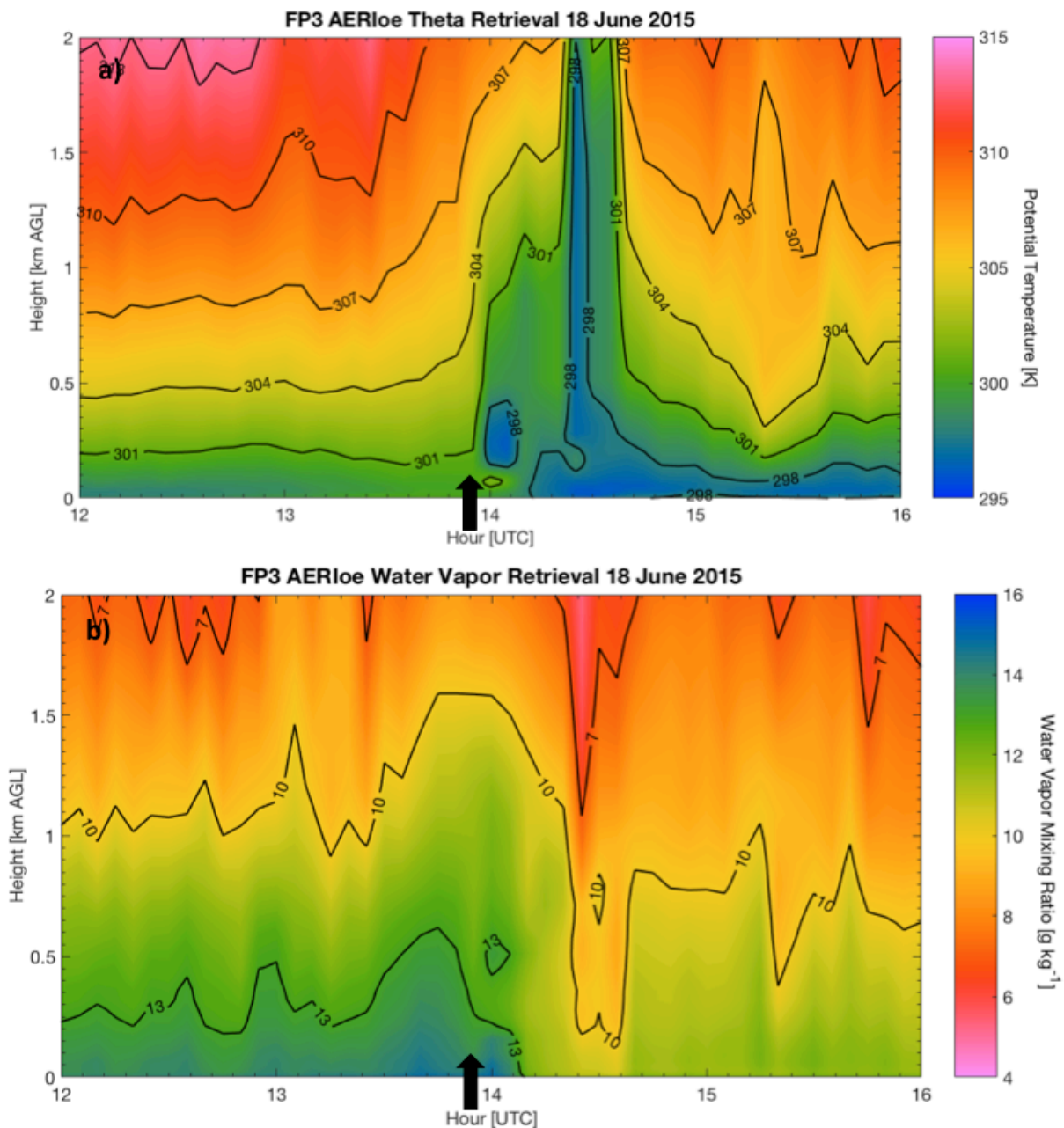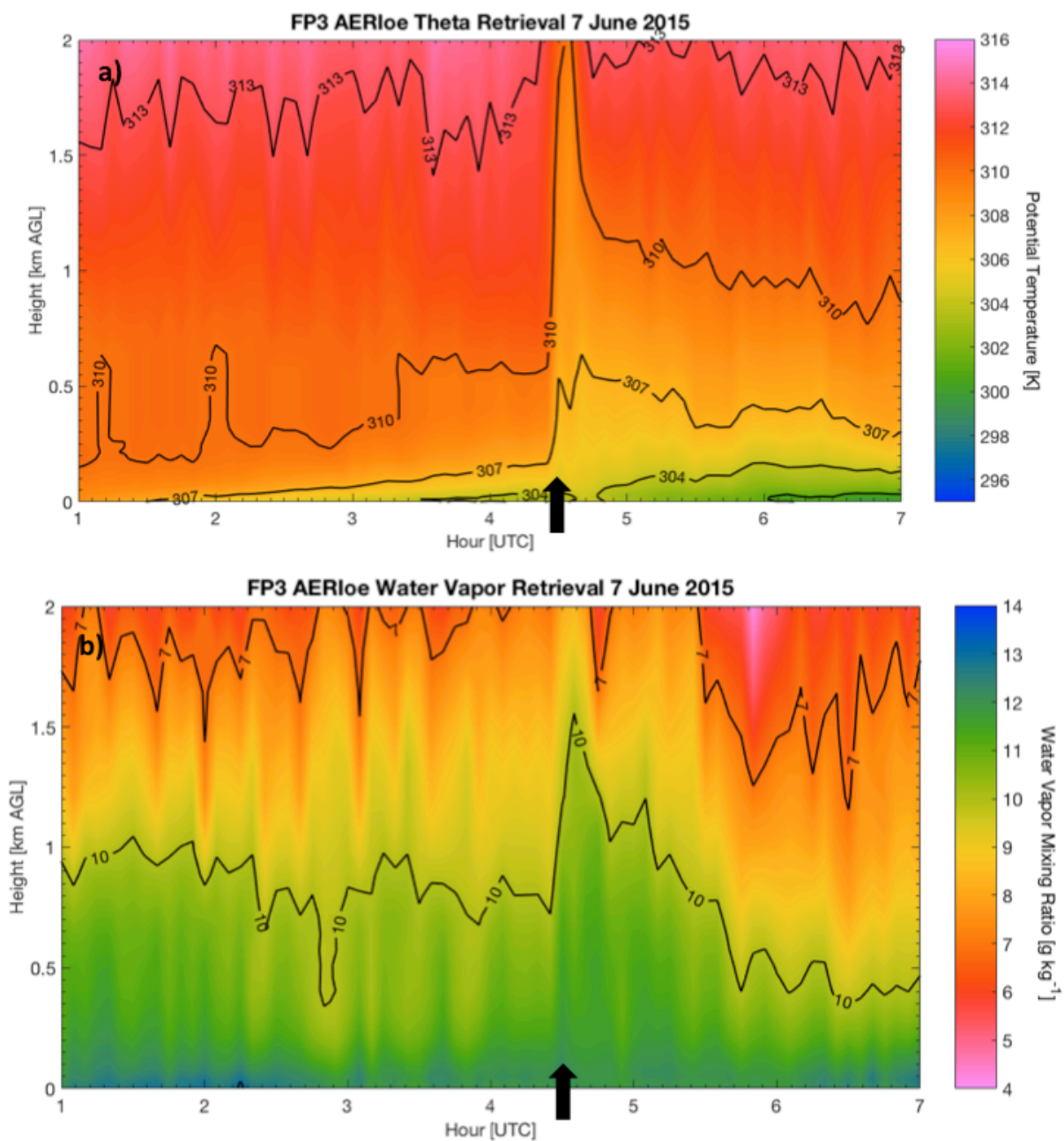
Figure 6.6: AERIoe retrieved a) potential temperature and b) water vapor mixing ratio time-height cross-section from FP3 in Ellis, KS from 7 June 2015 from 0100 UTC to 0700 UTC. Potential temperature and water vapor mixing ratio is shaded, with isentropes and isohumes outlined and labeled every 3 K and 3 g kg^{-1}. The bore start time is 0430 UTC, denoted by the black arrows.
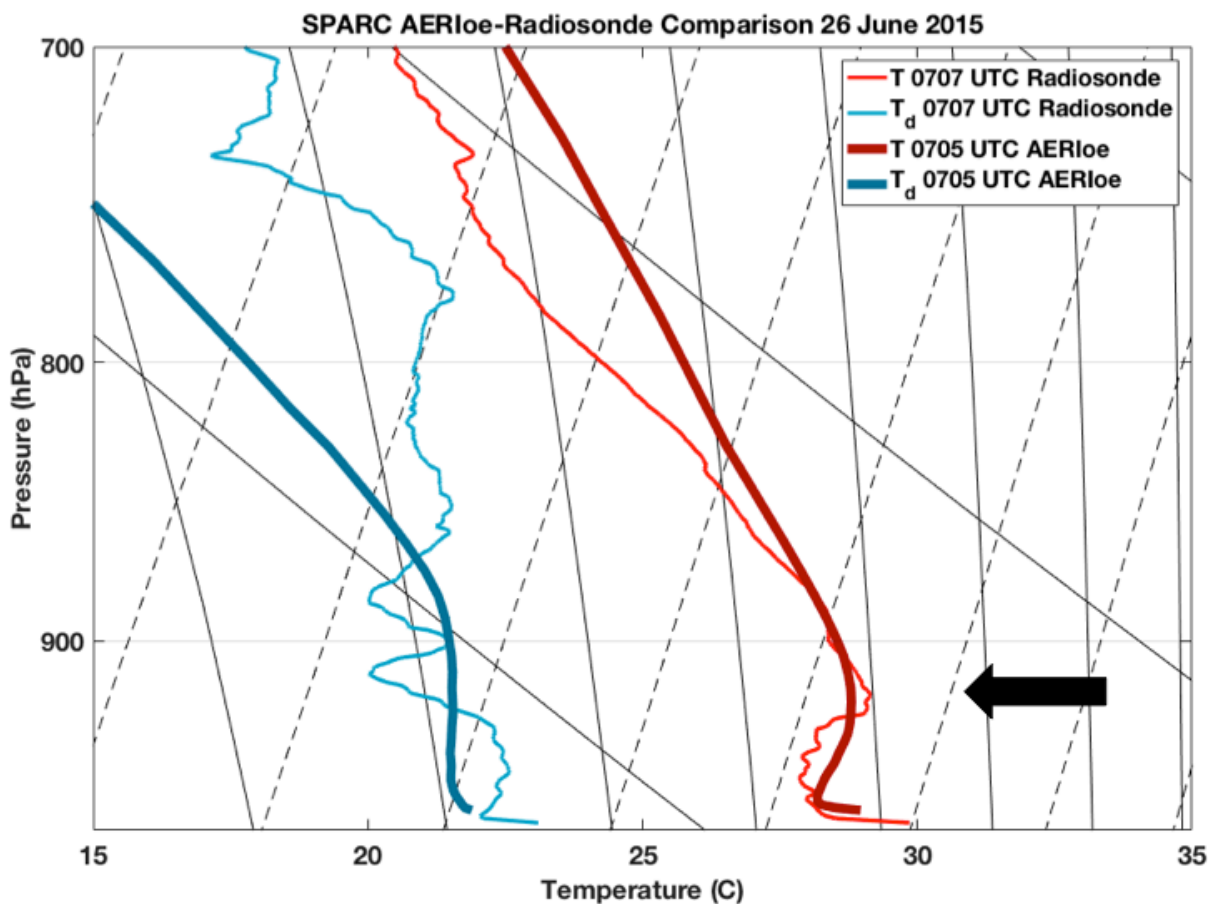
Figure 6.7: Radiosonde temperature (thin, red) and dew point temperature (thin, teal) comparison with AERIoe retrieved temperature (thick, red) and dew point temperature (thick, teal) skew-T/log-P graph for a pre-bore radiosonde on 26 June 2015 from MP3 (SPARC). Pre-bore inversion is located around 925 hPa, highlighted by the arrow.
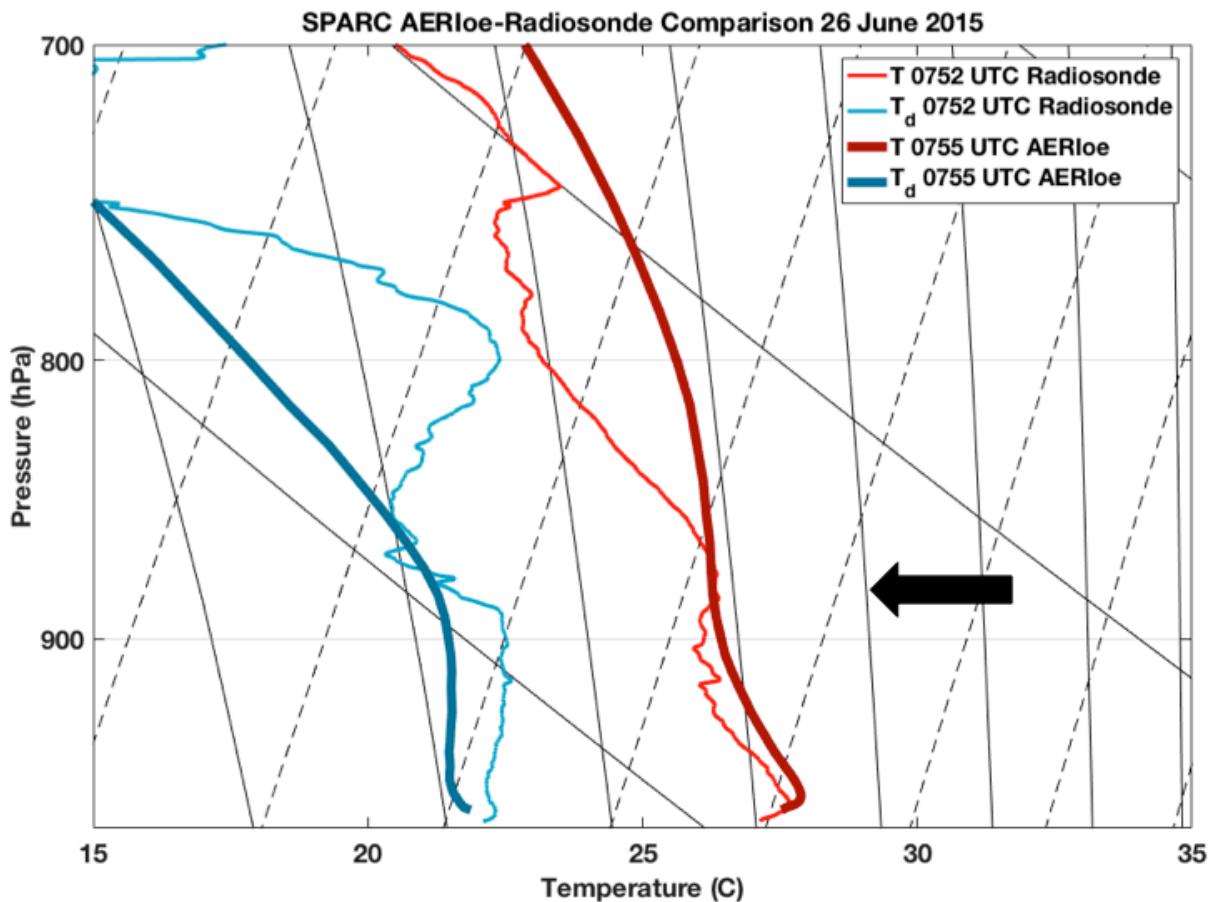
Figure 6.8: Radiosonde temperature (thin, red) and dew point temperature (thin, teal) comparison with AERIoe retrieved temperature (thick, red) and dew point temperature (thick, teal) skew-T/log-P graph for a post-bore radiosonde on 26 June 2015 from MP3 (SPARC). Post-bore inversion is lifted to around 875 hPa, highlighted by the arrow. Near-surface inversion is a result of the gravity current arriving at the time of the radiosonde launch.

VII. Composite Analysis

One of the drawbacks of current available literature available on bores is that all observational studies have been case studies focused on a single bore. Previous studies have focused on bores that result in boundary layer transitions favorable for convective initiation and bores that result in convective initiation, primarily because they have the largest impacts and are most interesting for the sake of a case study. By creating a composite including both bores that are favorable and bores that are unfavorable for convective initiation, the mean changes within the boundary layer caused by a bore passage can be identified and the role of bores in convective initiation can be better identified. Since the composite will average conditions in both pre- and post-bore environments and show changes relative to the time that the bore passed overhead, the time of the bore passage must be defined through the use of an objective procedure.

A total of 20 bores were observed by the FP3, FP4, FP5, CLAMPS, and SPARC observing platforms during PECAN. There were likely more bores to pass over these sites, but they either occurred in proximity to rain or were too close to the density current to be distinguished as a bore. Table 3 displays the 20 bores included in this study from these observation platforms; note that the same bore observed at different times by multiple platforms is counted as an additional case.

Table 3: List of bores included in this study.

Date	Time [UTC]	Platform
2 June	0800	FP4
2 June	0940	FP3
3 June	1145	FP3
4 June	1025	FP3
7 June	0430	FP3
7 June	0530	FP4
8 June	0351	CLAMPS
8 June	0455	SPARC
17 June	0405	SPARC
17 June	0447	CLAMPS
18 June	1400	FP3
20 June	1155	FP4
21 June	1150	FP4
26 June	0455	FP3
26 June	0651	CLAMPS
26 June	0735	SPARC
1 July	0945	SPARC
12 July	0340	FP3
14 July	0545	FP5
16 July	0445	SPARC

A.   Developing the Composite

By considering factors related to bores, such as surface pressure, vertical velocity profiles, horizontal wind speed and direction (at the surface and profiles), and potential temperature profiles, a time range is identified in which a bore occurred. This time range is manually determined given knowledge of expected temporal changes in these atmospheric variables. Given the time range, thermodynamic retrievals from the AERIoe can be used to determine the exact time of bore passage by finding the time that the temporal rate of change of potential temperature is most negative between 200 m and 1000 m AGL. Potential temperature is averaged across that height range, and a time series of average potential

temperature between 200 m and 1000 m is created. A center difference averaging method is used to calculate the rate of cooling:

$$\frac{d\theta}{dt}(t_2) = \frac{\theta(t_1) - \theta(t_3)}{t_3 - t_1}$$
eq. (7)

where $t_1 < t_2 < t_3$. The time of greatest cooling (minimum in $\frac{d\theta}{dt}$) is declared to be the time of the bore passage. By identifying a specific time range in which a bore may have passed, gravity currents and precipitation are excluded, which would otherwise result in cooling rates similar to or greater than those caused by bore passages. While a more sophisticated bore identification procedure could be developed, including objective analysis of surface pressure changes and wind shifts, which is beyond the scope of this research.

B.   Composite Analysis Results

With a technique to identify the time of the bore passage, composite means can be calculated. Figure 7.1 displays the composite mean change in potential temperature with time (using Equation 7 above) averaged across the 0.2 km to 1.0 km layer, along with the composite mean average vertical velocity across the same vertical layer. Since the minimum in the change in potential temperature with time was the defining criterion for the time of the bore, vertical velocity has no bearing on the determination of the time of the bore and is measured by a different instrument from the AERI. The peak in vertical velocity, across the 0.2 km to 1.0 km layer, coincides with the minimum in the change in potential temperature (greatest cooling) at time zero (the objectively determined time of bore passage). This engenders confidence in the compositing method, as the wind profilers independently identify the bore's leading updraft at the same time the AERI has been identifying cooling.
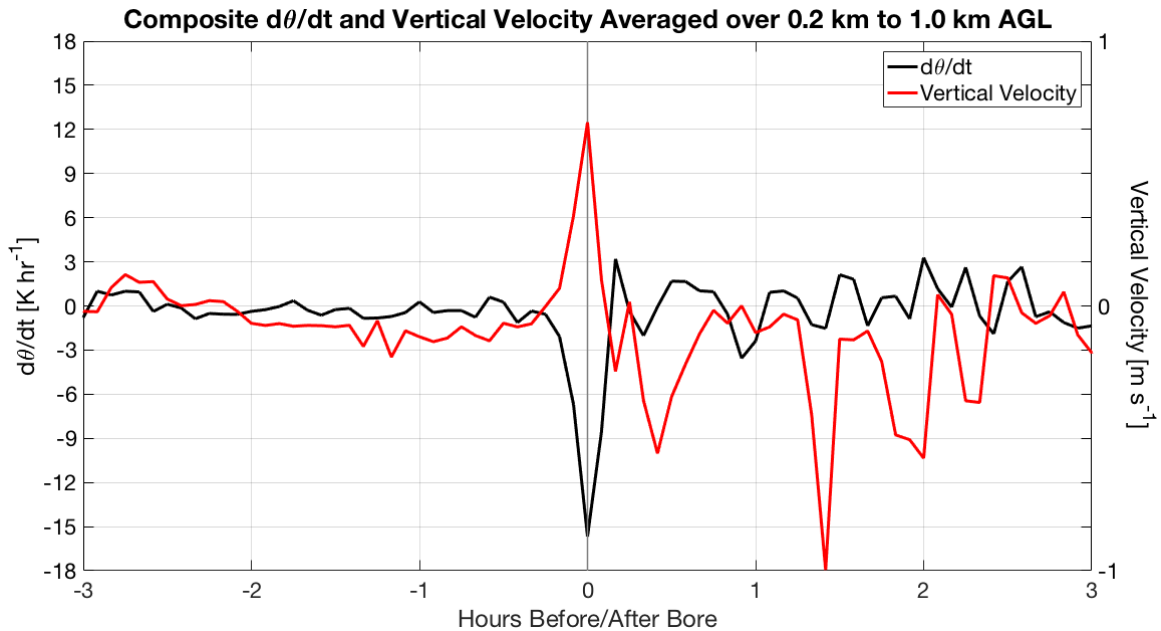
Figure 7.1: Composite mean change in potential temperature with time averaged over the 0.2 km to 1.0 km layer (plotted in black, left axis) and composite mean vertical velocity averaged over the 0.2 km to 1.0 km layer (plotted in red, right axis).

Figure 7.2 displays the time-height cross-section of the composite mean AERIoe-retrieved potential temperature, and reveals isentropic ascent at the time of the bore passage. Maximum composite mean parcel displacements are on the order of 700 m, similar to parcel displacements observed in previous case studies (e.g. Weckwerth et al. 2004). This composite structure qualitatively resembles a bore, which gives confidence in the compositing technique. The AERIoe potential temperature retrieval composite reveals near-surface cooling of about 1 K with the bore passage while the surface temperature composite (measured with surface meteorology stations, and not the AERIoe), displayed in Figure 7.3, shows negligible temperature changes with the bore passage. This aligns with previous observations, which have shown that bores are characterized by either warming at the surface (Clarke et al. 1981), or negligible surface temperature changes (Mahapatra et al. 1991).

Figure 7.2 shows more significant cooling approximately one hour after the bore passage, which would be from gravity currents trailing the bores.
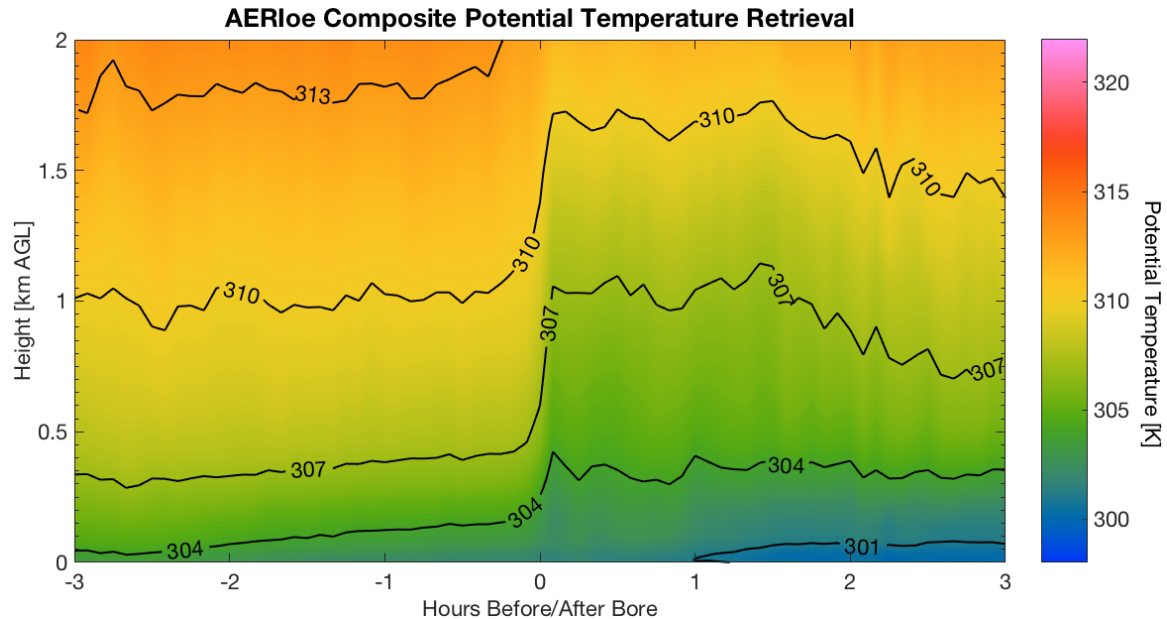
Figure 7.2: Composite mean AERIoe potential temperature retrieval. Isentropes labeled every 3 K.

Figure 7.4 displays the variability of changes in surface temperature and dew point temperature. This is calculated by averaging the variable for 1 hour before and after the bore, and finding the difference between the two averages. The mean differences are very close to zero change in both surface temperature and dew point temperature. Additionally, the majority of cases have changes within ± 1 °C. However, some cases do exhibit changes greater than ± 2 °C across the one hour averaging periods, which is somewhat more significant warming/cooling and moistening/drying than the composite alone indicates. Surface warming and negligible surface temperature changes are typical of bores, but they should not result in cooling. The cooling would be due to the arrival of gravity currents behind the bore, resulting in cooler temperatures being included in the one hour averaging.
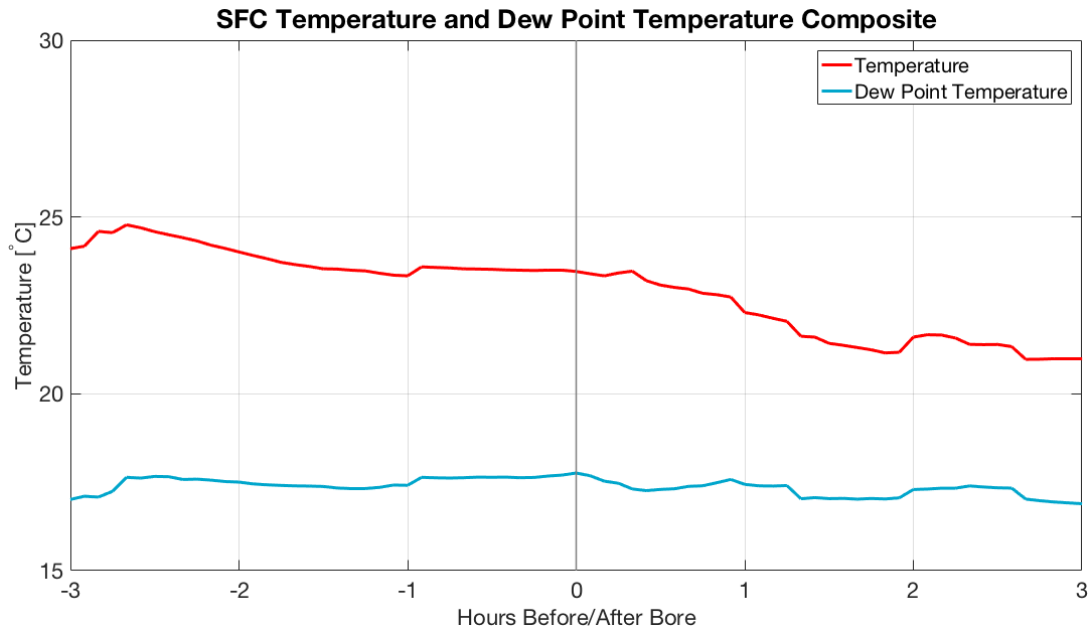
Figure 7.3: Composite mean surface temperature (red) and dew point temperature (blue).
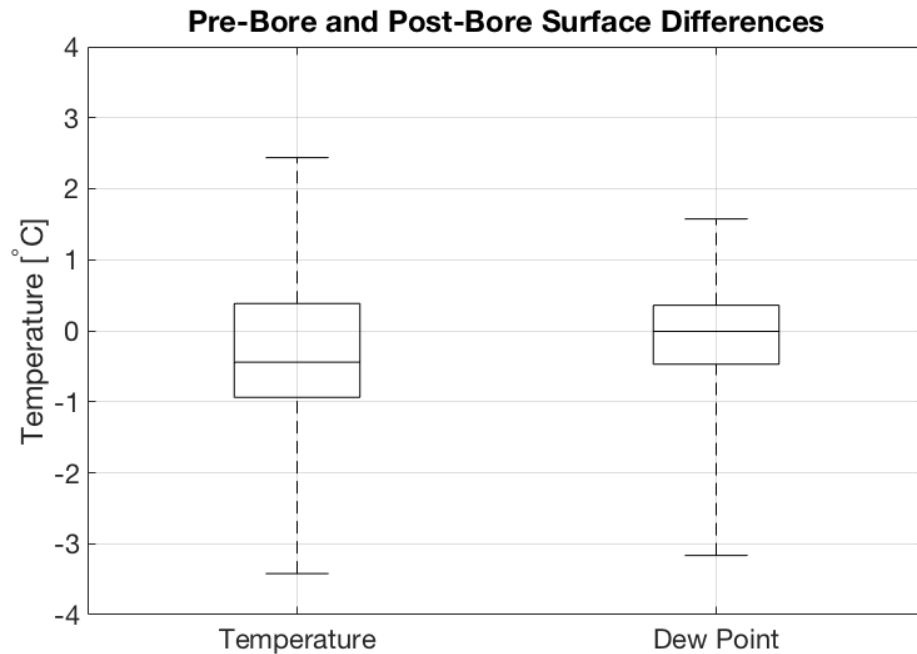
Figure 7.4: Pre-bore and post-bore surface temperature and dew point temperature are averaged over the course of 1-hour prior to and after the bore, respectively. Differences are calculated taking post-bore variable average minus pre-bore variable average such that a positive change means that the bore is observed to induce an increase in the respective variable with its passage. Box edges are at the first quartile and third quartile, with median value plotted with a horizontal line, whiskers extend to the minimum and maximum of the sample.

The time-height composite mean cross-section of the vertical velocity retrievals from the radar wind profilers and Doppler lidars used at each site is shown in Figure 7.5. An updraft on the order of $1 - 2$ m s^{-1} is identified at the leading edge of the bore. The first undulation in the composite can be identified as a downdraft about 20 minutes after the bore. Beyond this first updraft/downdraft couplet, trailing undulations are unable to be identified in the vertical velocity composite. This is likely because 1) not all cases were undular in their appearance, which would result in reducing the signal with the averaging, and 2) the bores will not have the same periodicity and speed, and thus undulations will be occurring at different times behind the bore resulting in the signals of those weaker trailing solitary waves being averaged out. The stronger downdrafts that occur more than one hour after the bore are likely due to a reduction in the number of cases that have observations that persist that long after the bore (since mobile units often ended their operations shortly after bore passage), and several cases observed rain, and thus strong downdrafts, after the bore. Figure 7.6 displays the composite mean surface pressure, observed by surface meteorological stations. The composite mean surface pressure increases by 1.5 hPa within 20 minutes of the bore, consistent with bore passages observed by Clarke et al. (1981), Karyampudi et al. (1995), Koch and Clark (1999), and Koch et al. (2008). Figure 7.7 shows the horizontal wind speed composite as observed by the wind profilers and Doppler lidars. A low-level jet of around 17 m s^{-1} can be identified in the pre-bore conditions in the composite at 300 m AGL. The low-level jet (LLJ) has previously been identified as a typical wave trapping mechanism (Crook 1988, Koch et al. 1991). It gets lifted with the bore passage, but cannot be identified after the bore passage. This is likely due to the varying heights to which the LLJ is lifted, resulting in wind speed maxima being averaged out in the composite. There appears to be some evidence

of it around 1,000 m AGL at the time of the bore passage, but it is difficult to identify in the composite.
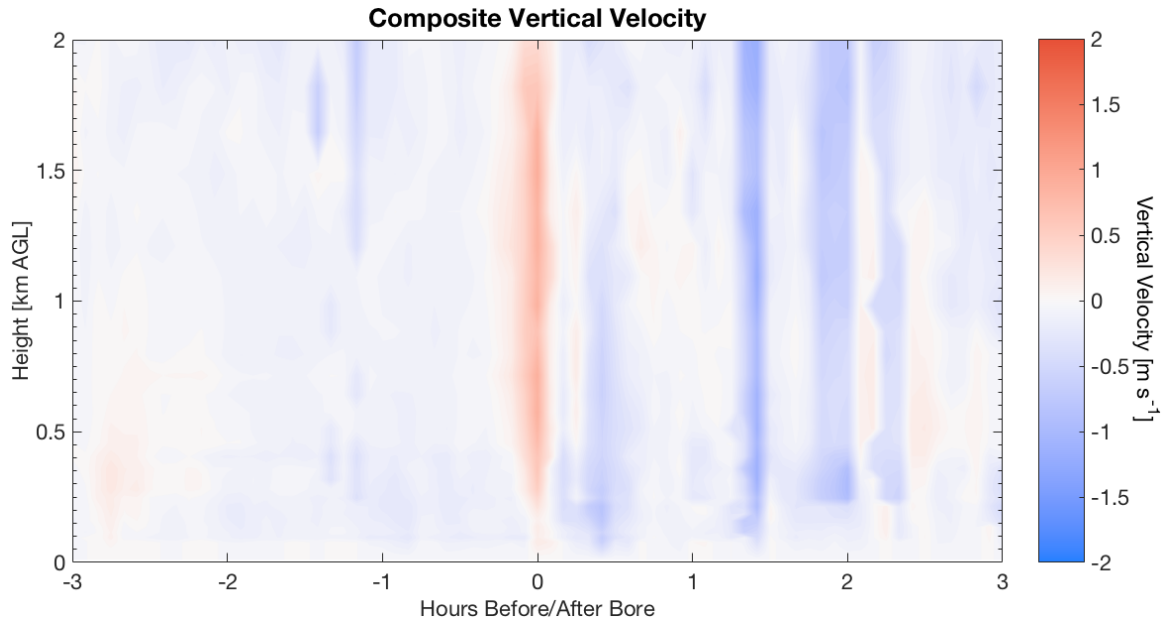
Figure 7.5: Composite mean vertical velocity as measured by 449, 915 MHz wind profilers and Doppler lidars.
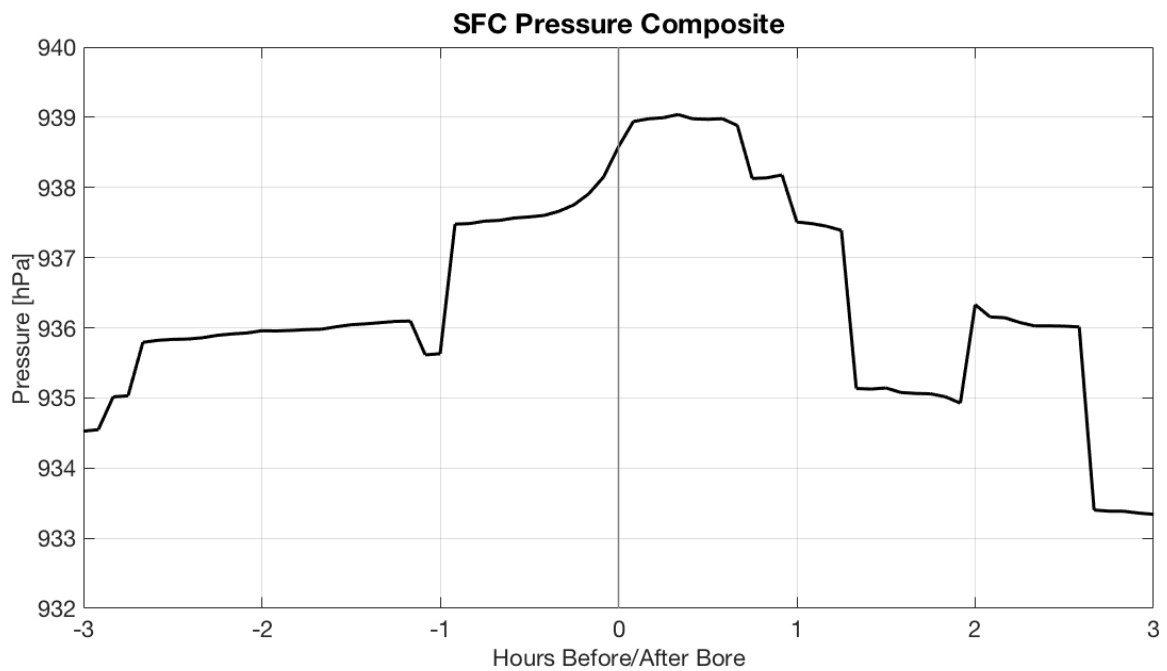
Figure 7.6: Composite mean surface pressure.

Wind Profiler Composite Wind Speed
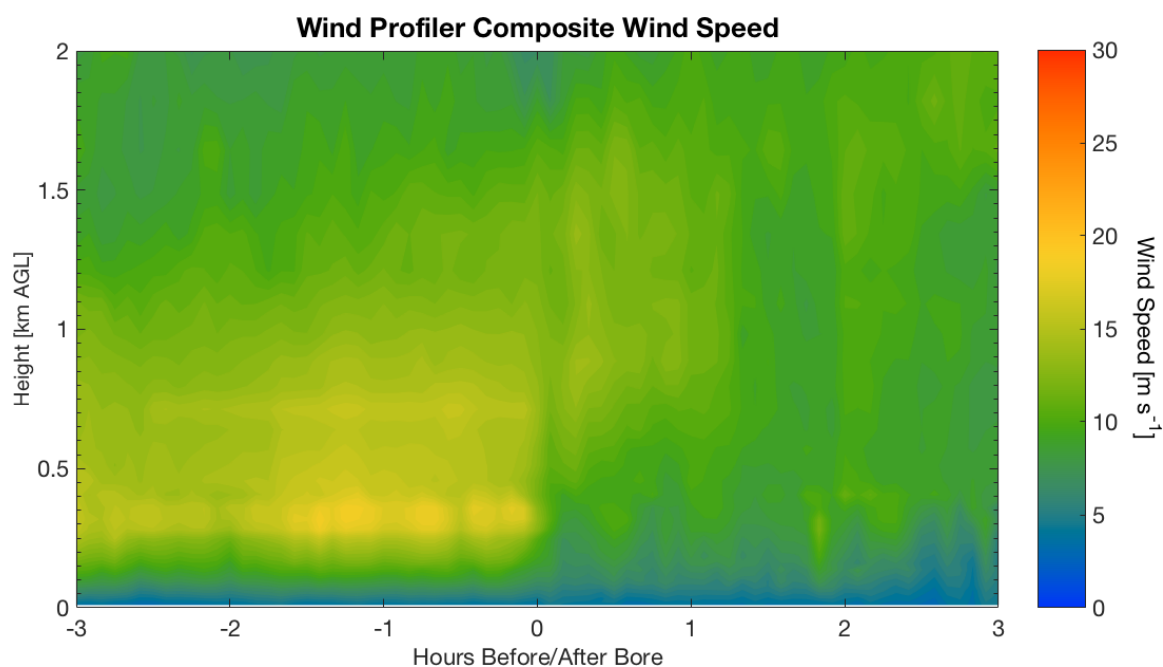
Figure 7.7: Composite mean horizontal wind speed as measured by 449, 915 MHz wind profilers and Doppler lidars.

The composite mean water vapor retrieval from the AERIoe is displayed in Figure 7.8. As was shown in both the previous section and Koch et al. (2008), bores can result in a rapid moistening or drying of the boundary layer. Figure 7.8 shows that there is an increase in moisture in the boundary layer with the bore passage. The 12 g kg^{-1} isohume is lifted about 200 m with the bore passage. This is much less than the 7 June 2015 case observed at FP3, shown in Figure 6.6 in the previous section. This is to be expected since the averaging includes bores that both moisten the boundary layer (e.g. 7 June 2015, shown in Figure 6.6) with those that rapidly dry the boundary layer (e.g. 18 June 2015, shown in Figures 6.5). With this composite, it can be inferred that of the 20 bores identified and included in the study during PECAN, bores were somewhat more likely to result in lofting of moisture in the boundary layer than rapidly drying the boundary layer. Koch et al. (2008) identified that the stronger mixing – which would result in drying of the boundary layer by mixing dry air from

the free troposphere down to the surface – occurs earlier in the bore's life cycle while weaker mixing, and thus moistening throughout the boundary layer, occurs near the end of the bore's life cycle. Given that bores early in their life cycle are more likely to be located near their parent gravity current and the precipitation that engendered it, and that AERI is unable to observe radiances in the presence of precipitation, this composite is likely biased towards late-life-cycle bores that have propagated away from the parent convection. Additionally, the stronger mixing cases will only result in rapid drying of the boundary layer if the free troposphere is sufficiently dry, which may not have always been the case for the bores included in this study.

Figure 7. 8: Composite mean AERIoe retrieved water vapor. Isohumes labeled every 1 g kg^{-1}.

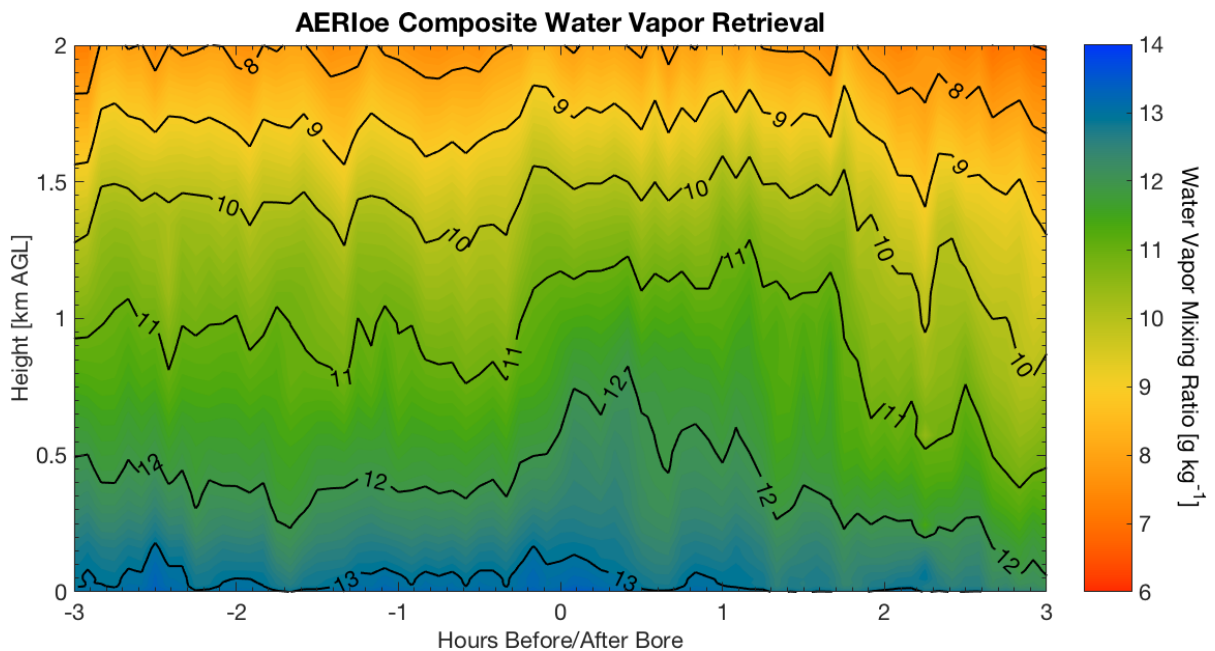## C.   Convective Indices

AERIoe-derived thermodynamic soundings provide the opportunity to assess trends in convective indices at high-temporal resolution. There is historical precedence for using

AERI-derived retrievals to monitor trends in convective indices, for using AERIs in bore studies, and monitoring time series of convective indices in bore case studies (albeit without an AERI). Feltz et al. (2002) used AERI-derived thermodynamic profiles to calculate severe indices during the 3 May 1999 Kansas and Oklahoma tornado outbreak. Wagner et al. (2008) observed the temporal evolution in severe convective indices for tornadic and non-tornadic supercell environments, from 1999 to 2003, using AERI-derived thermodynamic profiles. Coleman and Knupp (2011) showed time series of CAPE, CIN, and LFC height with a bore and soliton passage, using thermodynamic variables derived from a microwave radiometer. AERIoe would likely have a more accurate calculation of convective indices than microwave radiometers, given the increased vertical resolution as a result of a greater number of absorption bands in the infrared compared to the microwave. While severe index calculations using AERIoe profiles are unlikely to be exactly the same as coincident radiosondes due to smoothing and vertical resolution differences outlined earlier, trends in observed stability are still useful.

Using the same compositing method, we can analyze trends in convective indices to assess whether or not the bore passage is making the environment more or less likely to produce convection. To do this, the convective available potential energy (CAPE), convective inhibition (CIN), lifted condensation level (LCL), and level of free convection (LFC) are calculated for each individual case using the SHARPpy program (Blumberg et al. 2017) and then averaged together to form a composite time series. SHARPpy is a meteorological Python package available online (https://github.com/sharppy/SHARPpy) that uses the same methods to calculate severe indices as the National Oceanographic and

Atmospheric Administration's (NOAA) Storm Prediction Center's (SPC) operational forecasting software.

The composite time series of surface-based and most-unstable parcel CAPE is shown in Figure 7.9. Surface-based calculated indices use the surface parcel, while the most-unstable calculated indices finds the parcel that has the greatest CAPE and calculates the indices from that level. Surface-based CAPE (SBCAPE) has a gradual decrease throughout the time period of analysis, likely due to radiational cooling since all of the cases occurred during the overnight hours. With the passage of the bore, SBCAPE decreases at a slightly greater rate than prior to the bore. A similar trend is observed in the most-unstable parcel CAPE (MUCAPE), where the bore passage results in a greater rate of decrease than with SBCAPE. The most-unstable level does not change at all with the bore passage, staying at 870 m AGL around the time of the bore. It is unclear whether this is a product of the AERIoe retrievals or a real phenomenon as an insufficient number of pre- and post-bore radiosondes were available to determine this. As such, changes in MUCAPE are due to the changes at the most-unstable level and above, and not due to changes in the altitude of the most-unstable parcel.
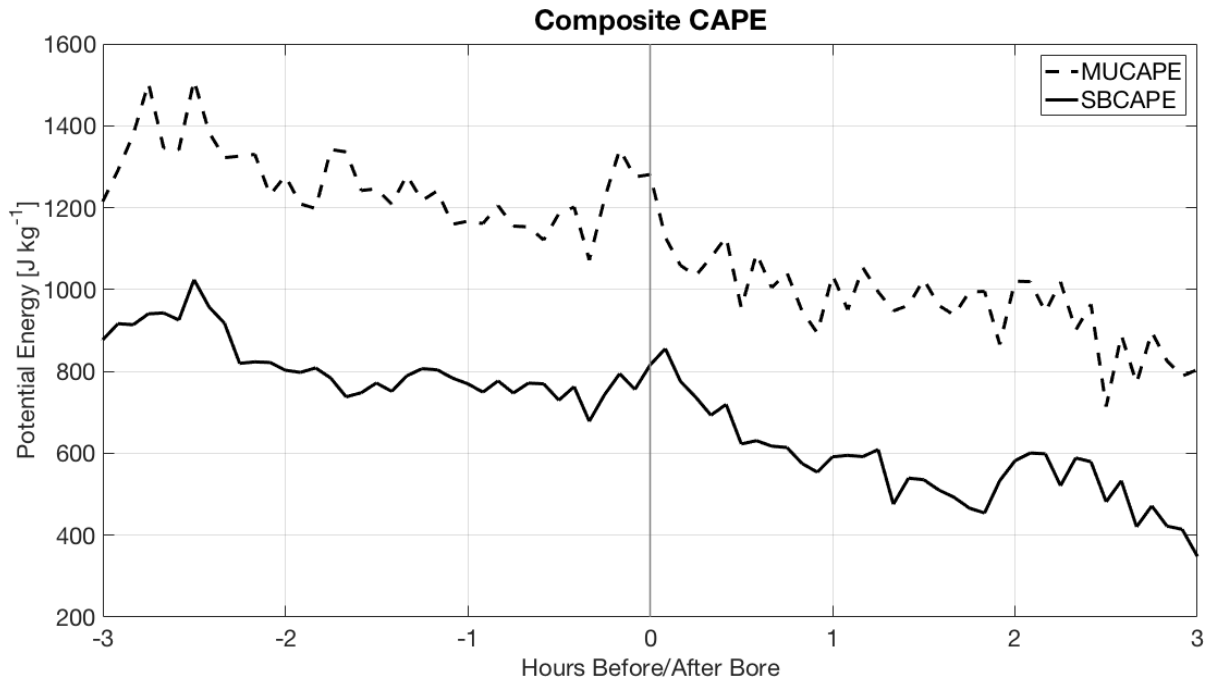
Figure 7.9: Composite mean time series of surface-based (solid line) and most-unstable parcel (dashed line) convective available potential energy (CAPE) relative to bore passage time.

Time series of surface-based and most-unstable CIN (SBCIN and MUCIN) are shown in Figure 7.10. SHARPpy outputs CIN as a negative value, but SBCIN and MUCIN are shown as absolute value of those quantities. For both SBCIN and MUCIN, there is a decrease of 50 to 100 J kg^{-1} immediately after the bore passage. After that, SBCIN increases back to pre-bore levels. MUCIN slowly increases again after the bore. Coleman and Knupp (2011) showed a rapid decrease in SBCIN coincident with an increase in SBCAPE as a bore passed. The decrease in SBCIN with the bore passage would allow for the environment to be more conducive to convection, but the decrease in SBCAPE would suggest any convection that initiated after the bore would be less intense than convection initiated in the pre-bore environment. The decrease in SBCIN is expected as a typical characteristic of bores is the

lifting, cooling, and weakening of the capping inversion (Koch et al. 1991, Koch and Clark 1999, Koch et al. 2008, Coleman and Knupp 2011).
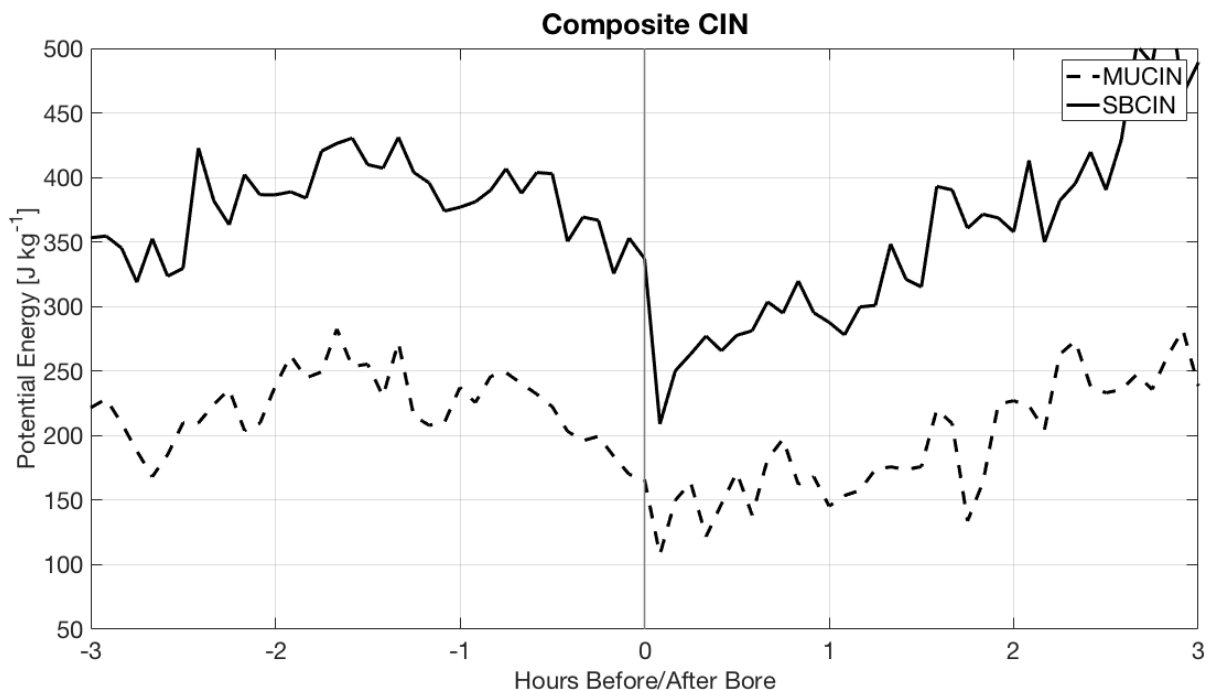
Figure 7.10: As in Figure 7.9 but for CIN.

Surface-based and most-unstable parcel LCL (SBLCL and MULCL) heights are displayed in Figure 7.11. SBLCL has a very gradual decrease over the time of the composite, decreasing from 1 km AGL to 0.7 km AGL, but the bore does not have an impact on the trend. The reason for this can be understood when considering the composite surface temperature and dew point temperature in Figure 7.3. While dew point temperature does not change over the time series, the temperature slowly decreases, which results in the persistent lowering of the SBLCL. The MULCL does decrease 300 m with the bore passage, likely due to the lower-level cooling associated with the bore. Additionally, the lofting of water vapor could play some role in lowering the MULCL. The composite mean water vapor retrievals (Figure 7.8) indicate more bores that loft moisture and moisten the boundary layer were

observed as compared to the cases that result in drying. The increase of moisture higher in the boundary layer, near the most-unstable level, would result in the lowering of the MULCL. This only indicates that the cloud base would be 300 m lower with the bore passage and does not necessarily give clues as to the convective potential.
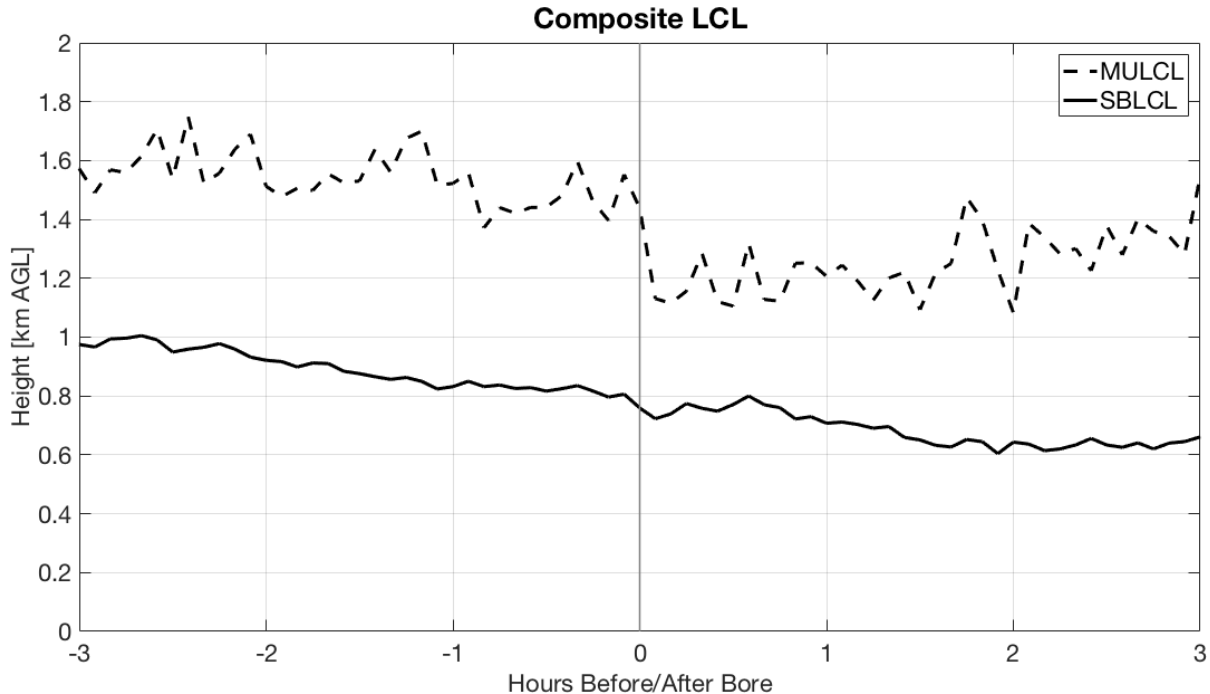
Figure 7.11: As in Figure 7.9 but for LCL height.

Composite mean surface-based and most-unstable LFC (SBLFC and MULFC) heights are displayed in Figure 7.12. Both SBLFC and MULFC heights display similar behavior across the time series. The LFC height drops about 500 to 700 m with the bore passage, going from about 3.3 km AGL to around 2.7 km AGL, reaching a relative minimum at or just after the time of the bore passage. The reduction in LFC height with the bore passage means that vertical motions induced by the bore passage have to lift parcels to a lower height, compared to the pre-bore environment, in order to initiate convection. This is significant considering the layer in which this bore-induced lifting is occurring is roughly

within the bottom 2 km AGL of the atmosphere. It is in this layer where low-level convergence (Figure 7.7) and vertical motions (Figure 7.5) are occurring. 3.3 km AGL would likely prove to be too high for bore induced lifting, but 2.7 km AGL is notably closer to the level where lifting is occurring. This decrease in LFC height is also expected since once again, lifting, cooling, and weakening of the capping inversion results a lower LFC height just as it does for reduced CIN (Koch et al. 1991, Koch and Clark 1999, Koch et al. 2008, Coleman and Knupp 2011).
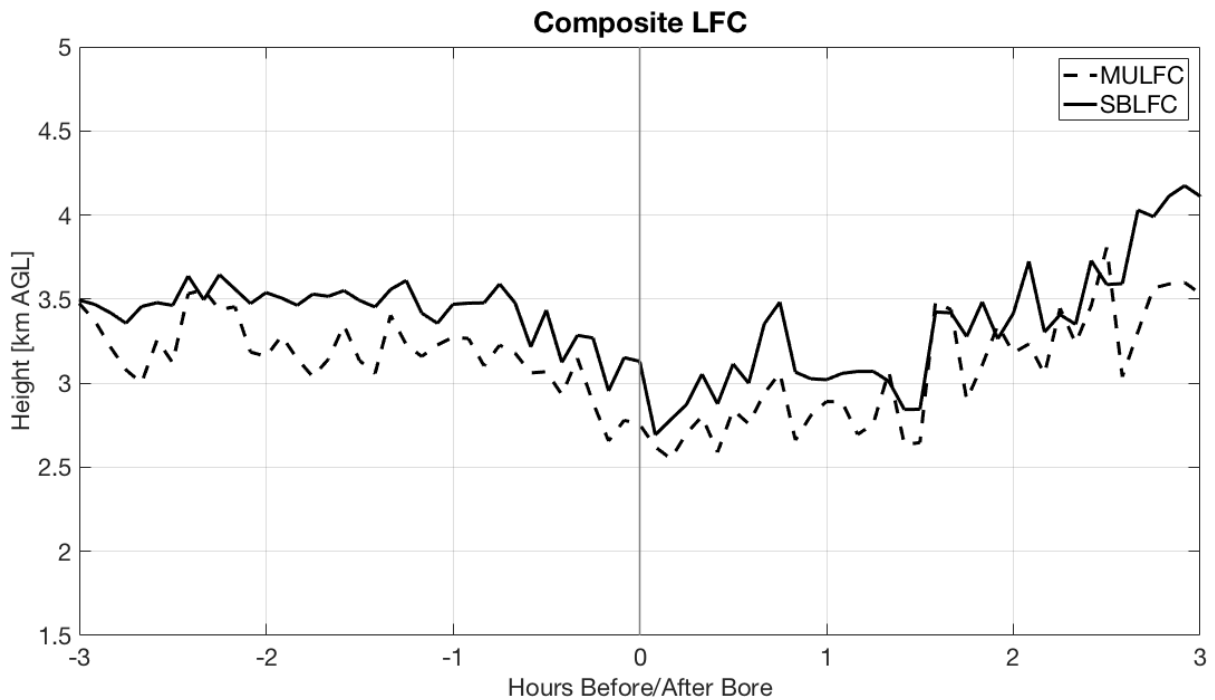
Figure 7.12: As in Figure 7.9 but for LFC height.

Figure 7.13 displays both a pre-bore radiosonde and a post-bore radiosonde launched by SPARC operators on 26 June 2015. The pre-bore radiosonde was launched at 0707 UTC while the post-bore radiosonde was launched at 0752 UTC, while the bore occurred at 0735 UTC. The pre-bore inversion is located at 925 hPa. In the post-bore sounding, the pre-bore inversion has been lifted dry adiabatically about 0.5 km to 875 hPa. These two radiosondes

are a great example of a bore lifting, cooling, and weakening the capping inversion, resulting in a decrease in CIN and LFC height, and thus increasing the potential for convective initiation behind the bore.
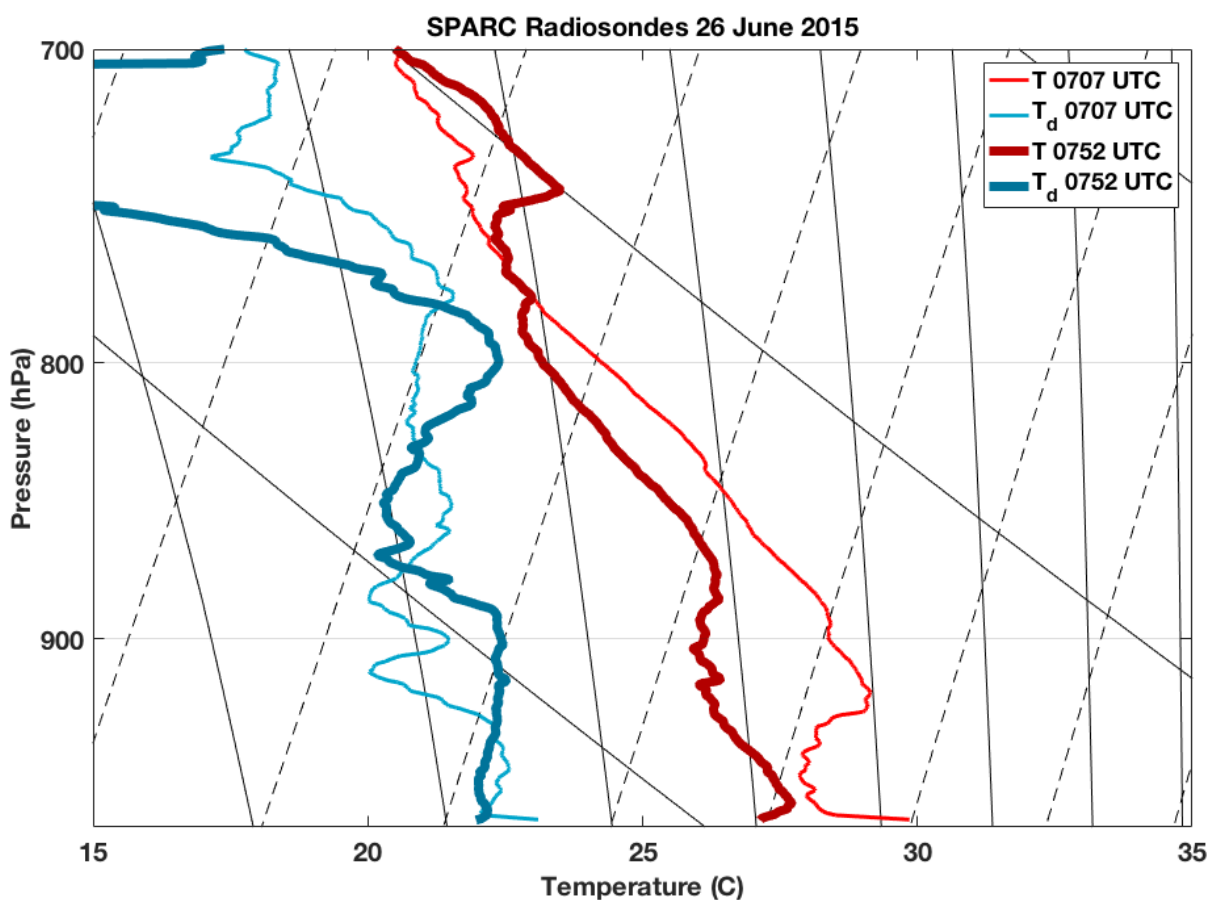
Figure 7.13: Pre-bore (0707 UTC, thin, light lines) and post-bore (0752 UTC, thick, dark lines) SPARC radiosondes on 26 June 2015. Bore occurred at 0735 UTC. Temperature is plotted in red, dew point temperature plotted in teal. Post-bore radiosonde has a near-surface inversion due to the arrival of the bore's parent gravity current at the time of the radiosonde launch.

Pre-bore and post-bore index differences were also investigated by averaging index values for the one hour periods that preceded and followed bore passage in order to compute an average pre- and post-bore index; these averages were calculated using each individual case instead of calculating indices from composite values. The difference was then defined as

post-bore minus pre-bore so that a positive difference would imply an increase in the particular severe index, similar to Figure 7.4. Figures 7.14 and 7.15 display the variability of changes to CAPE and CIN, and LCL and LFC height respectively. It is seen that the most-unstable parcel indices have greater variability than the surface-based parcel indices. In the majority of cases, SBCIN and MUCIN decrease with the bore passage, as do the MULCL and MULFC heights. SBCAPE and MUCAPE, along with SBLCL, have median differences near zero. It is shown that several cases exhibited positive trends in these indices, and several cases also exhibited negative trends. These indices also displayed little trend in the composite mean analysis, as previously shown in Figures 7.8 and 7.10. SBLFC also has a median value near zero, with most cases on the negative side of the zero-line, but the first quartile extends to the positive side of the zero-line. The slight downward trend with the bore passage, observed in the composite mean in Figure 7.12, could perhaps be partly explained by the very negative outlier, as shown in Figure 7.15. In general, Figures 7.14 and 7.15 show that bores tend to result in decreases in CIN and LFC height and MULCL heights, but can be quite variable with respect to changes in CAPE.
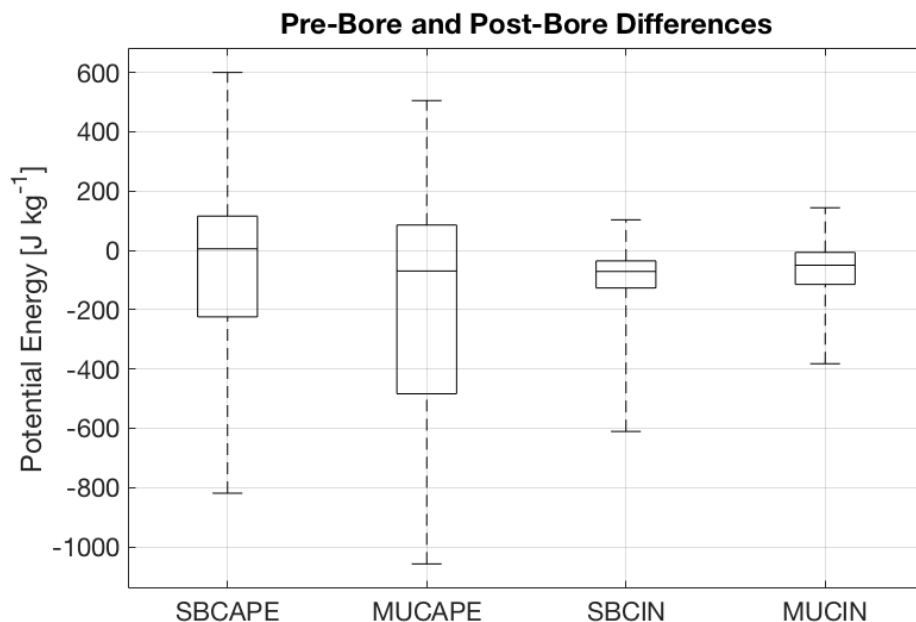
Figure 7.14: As in Figure 7.4 but for SBCAPE, MUCAPE, SBCIN, and MUCIN.
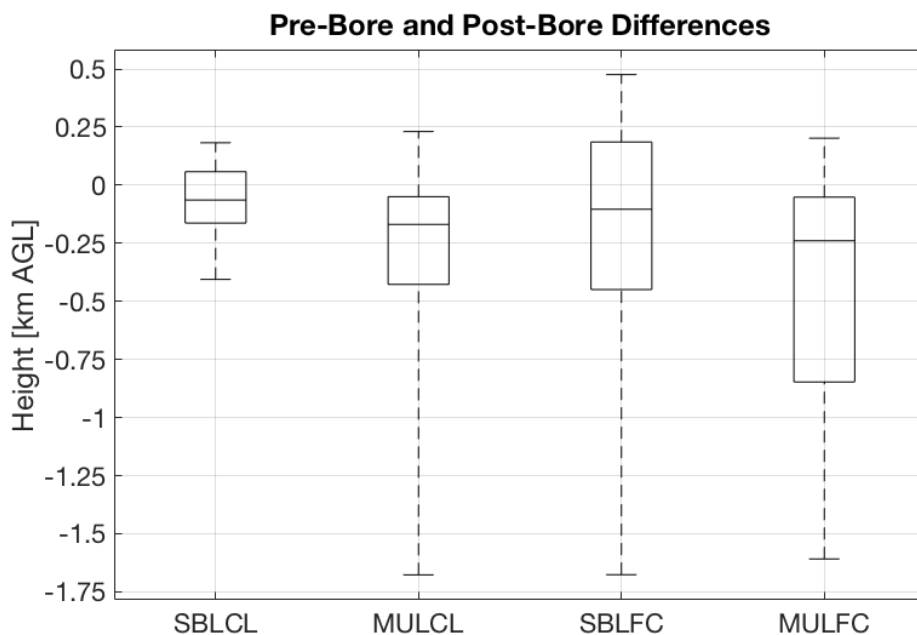
Figure 7.15: As in Figure 7.4 except for SBLCL, MULCL, SBLFC, and MULFC height.

Overall, the results presented here are mixed with respect to the problem of bores and convective initiation. The reduced CAPE, according to the composite mean analysis, would characterize weaker convection. However, Figures 7.10, 7.12, 7.14 and 7.15 display a greater

signal with the bore passage, and indicate most cases exhibit a reduction in LFC height and CIN. This trend would increase the potential for convective initiation to occur. Thus, in this composite mean sense, it appears that bores are likely to increase the potential for convective initiation but the reduced CAPE, in many of the cases, may indicate that the convection in the post-bore environment will be weaker in the pre-bore environment. It is important to note that a composite mean does not represent all bores, and individual bores have been observed to induce severe convection (eg. Karyampudi et al. 1995, Locatelli et al. 2002). However, it is also observed here that bores can stabilize the atmosphere, which has not necessarily been communicated in the literature.

VIII. Case Study Comparison

The large variability in changes to CAPE displayed in Figure 7.14, and especially the preference toward decreasing CAPE, is an interesting result. Both Koch et al. (2008) and Coleman and Knupp (2011) observed a "modest" increase of surface-based CAPE with a bore passage and Coleman and Knupp also observed an increase in 300 m CAPE. While a few cases exhibit an increase in CAPE, the majority of cases result in a decrease, something that has not been previously documented in the literature. In order to try to understand the large differences in SBCAPE with the bore passage, the events with the maximum SBCAPE difference (21 June FP4) and the minimum CAPE difference (26 June FP3) are examined in greater detail.

Figures 8.1 through 8.4 display time series of surface-based and most-unstable parcel calculations for CAPE (8.1), CIN (8.2), LCL height (8.3), and LFC height (8.4) for both the 21 June FP4 case and the 26 June FP3 case. As shown in Figure 8.1, SBCAPE increased by 1000 J kg^{-1} with the bore passage in the 21 June case, while MUCAPE increased to a maximum ahead of the bore, but then decreased again after the bore. For the 26 June case, SBCAPE and MUCAPE gradually decreased with time, with the appearance that the bore accelerated the rate at which CAPE decreased, similar to what was seen in the composite analysis in the previous section (Figure 7.9).

Figure 8.2 displays SBCIN and MUCIN for both cases. Note that SBCIN was undefined for the 21 June case prior to the bore, as there was zero SBCAPE at that time and CIN is undefined without positive CAPE. On 21 June, MUCIN decreased from about 600 J kg^{-1} to about 100 J kg^{-1} within the hour prior to the bore passage. The 26 June case exhibits

little change with the bore passage, with a short 10 – 15 minute time period of reduced CIN

right after the bore passage.
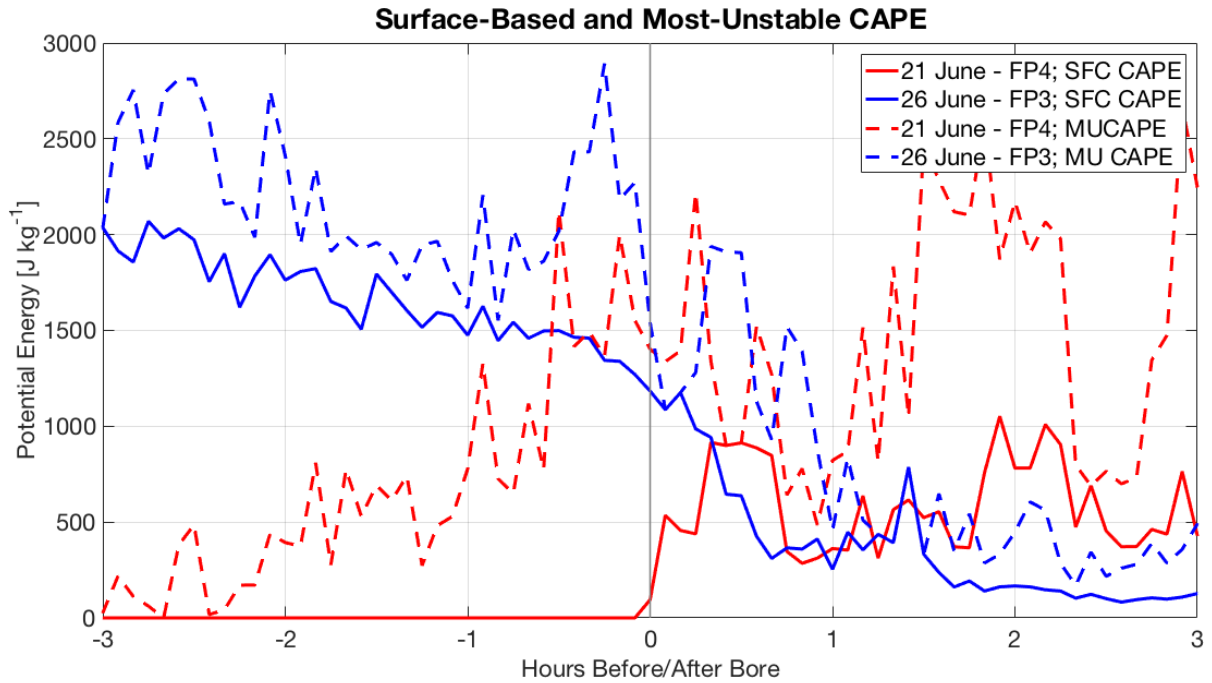
Figure 8.1: SBCAPE (solid line) and MUCAPE (dashed line) for a bore on 21 June 2015 at FP4 (red line) and 26 June 2015 over FP3 (blue line). Time shown is relative to the time of the bore, using the bore start time algorithm from section 7A. The 21 June FP4 bore occurred at 1150 UTC, and the 26 June FP3 bore occurred at 0455 UTC.
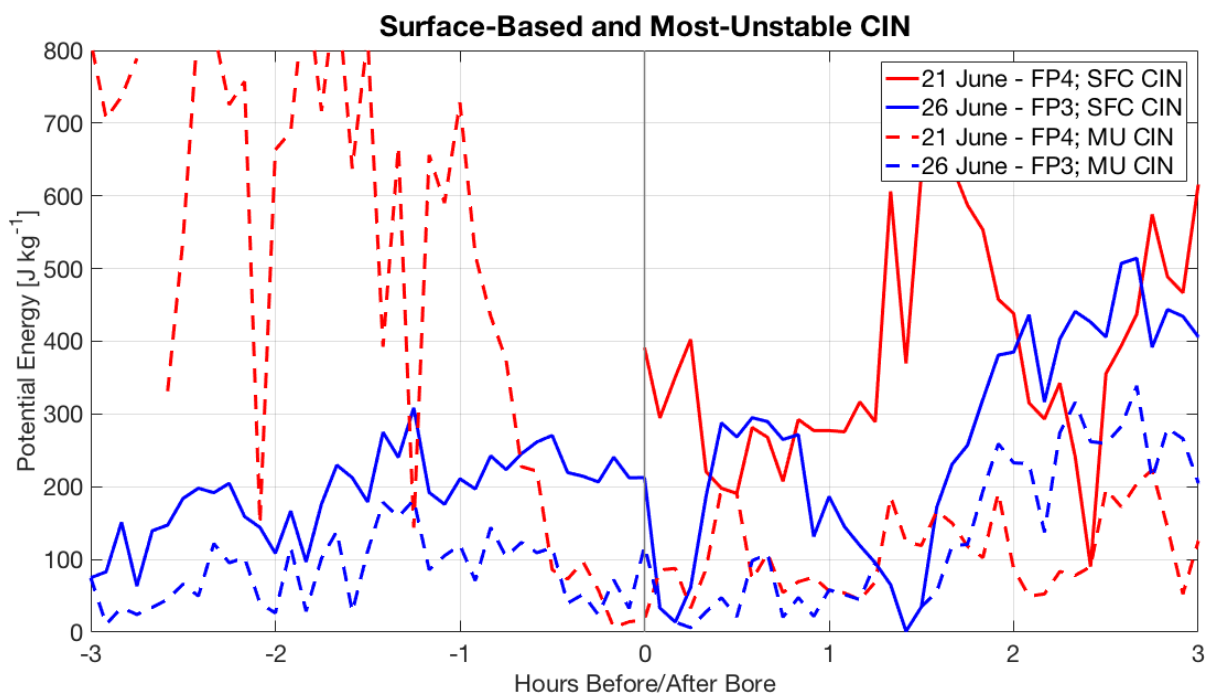
Figure 8.2: As in Figure 8.1 but for CIN instead of CAPE. Note: CIN is undefined when CAPE is zero. Large spikes in MUCIN for the 21 June case prior to the bore are likely due to noise in the AERIoe retrievals resulting in particularly large changes in the most-unstable parcel.

SBLCL height (Figure 8.3) changed little for both cases. MULCL height for the 26 June case shows negligible changes with the bore passage, but the 21 June case had a decrease of about 500 m for the 30 minutes following the bore passage. Figure 8.4 displays SBLFC and MULFC heights for both cases. LFC height cannot be calculated when CAPE is zero, so the 21 June case had no surface-based LFC height prior to the bore passage. In the 26 June case, the MULFC height stayed very similar in height across the bore passage, with an increase of about 500 m in the surface-based LFC height. We can only observe the time series of the MULFC height in the 21 June case because of the lack of pre-bore SBCAPE for that case. The 21 June case had a decrease of 3000 m in the hour prior to the bore passage; recall the gradual increase in most-unstable CAPE and decrease in MUCIN in that time

frame. This was due to surface heating as the bore is occurring at 1150 UTC (6:50 am local time) while sunrise was at 1105 UTC. Overall, the 21 June bore, coupled with diabatic surface heating, destabilized the environment while the 26 June bore stabilized it.
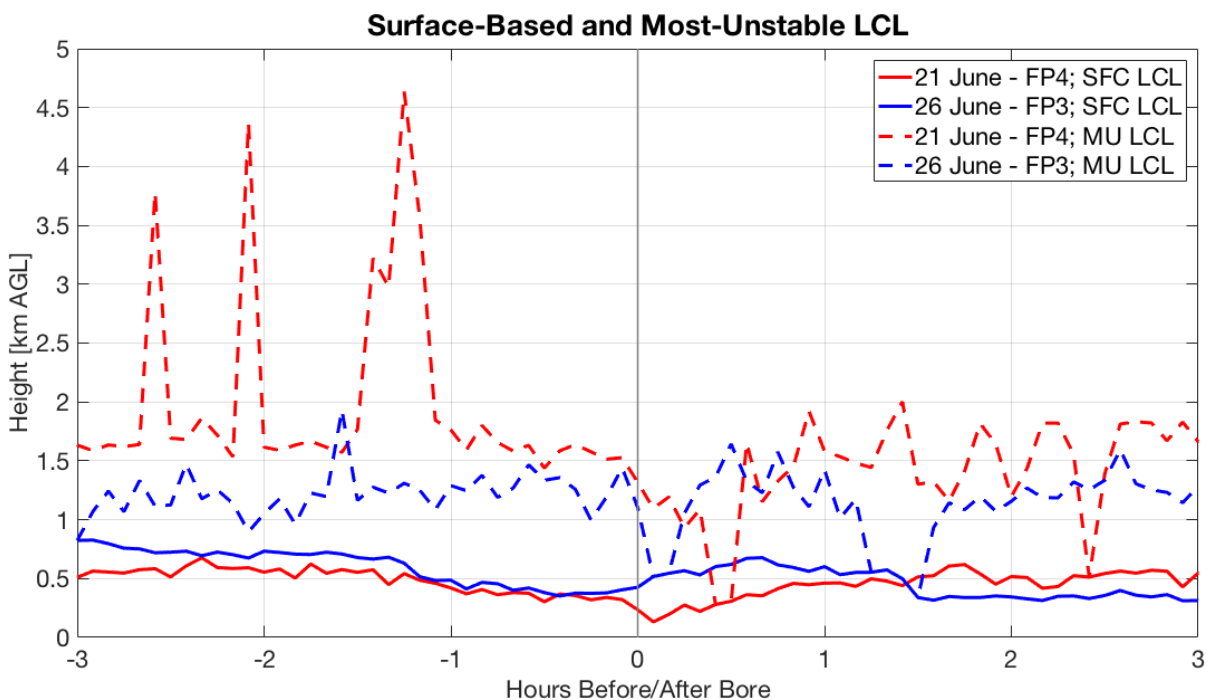
Figure 8.3: As in Figure 8.1 but for LCL height instead of CAPE. Large spikes in MULCL for the 21 June case prior to the bore are likely due to noise in the AERIoe retrievals resulting in particularly large changes in the most-unstable parcel.

The changes in severe indices shown in Figures 8.1 through 8.4 could be put into perspective when considering the AERIoe potential temperature and water vapor mixing ratio retrievals. Figures 8.5a and 8.6a display the potential temperature retrievals from the AERIoe for 21 June and 26 June respectively, while Figures 8.5b and 8.6b display the corresponding water vapor mixing ratios. The potential temperature retrievals show the bore front at 1150 UTC and 0455 UTC respectively. The real difference between the two cases is seen in the water vapor mixing ratio retrievals as the 21 June case resulted in lofting of moisture in the boundary layer, while the 26 June case resulted in a drying of the boundary

layer. Intuitively, this reduction in boundary layer moisture would increase the stability of the atmosphere, which is reflected in the severe indices. This would suggest that the "active phase" and "dissipation stage" of bores (Koch et al. 2008) could potentially play an important role in determining the potential for convective initiation behind the bore. While this is only a comparison between two cases, it would suggest that further investigation into the different mixing phases of the bore would provide additional insight to the problem of bores and their role in convective initiation.
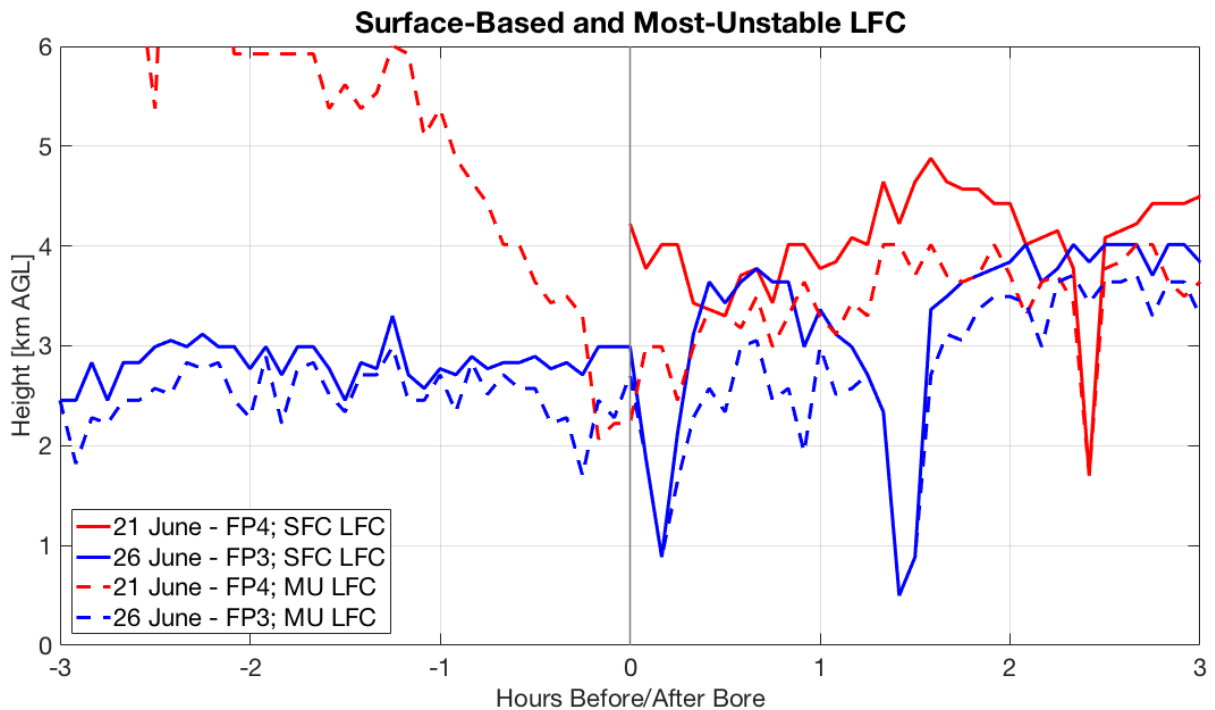
Figure 8.4: As in Figure 8.1 but for LFC height instead of CAPE. LFC is not available when CAPE is zero.
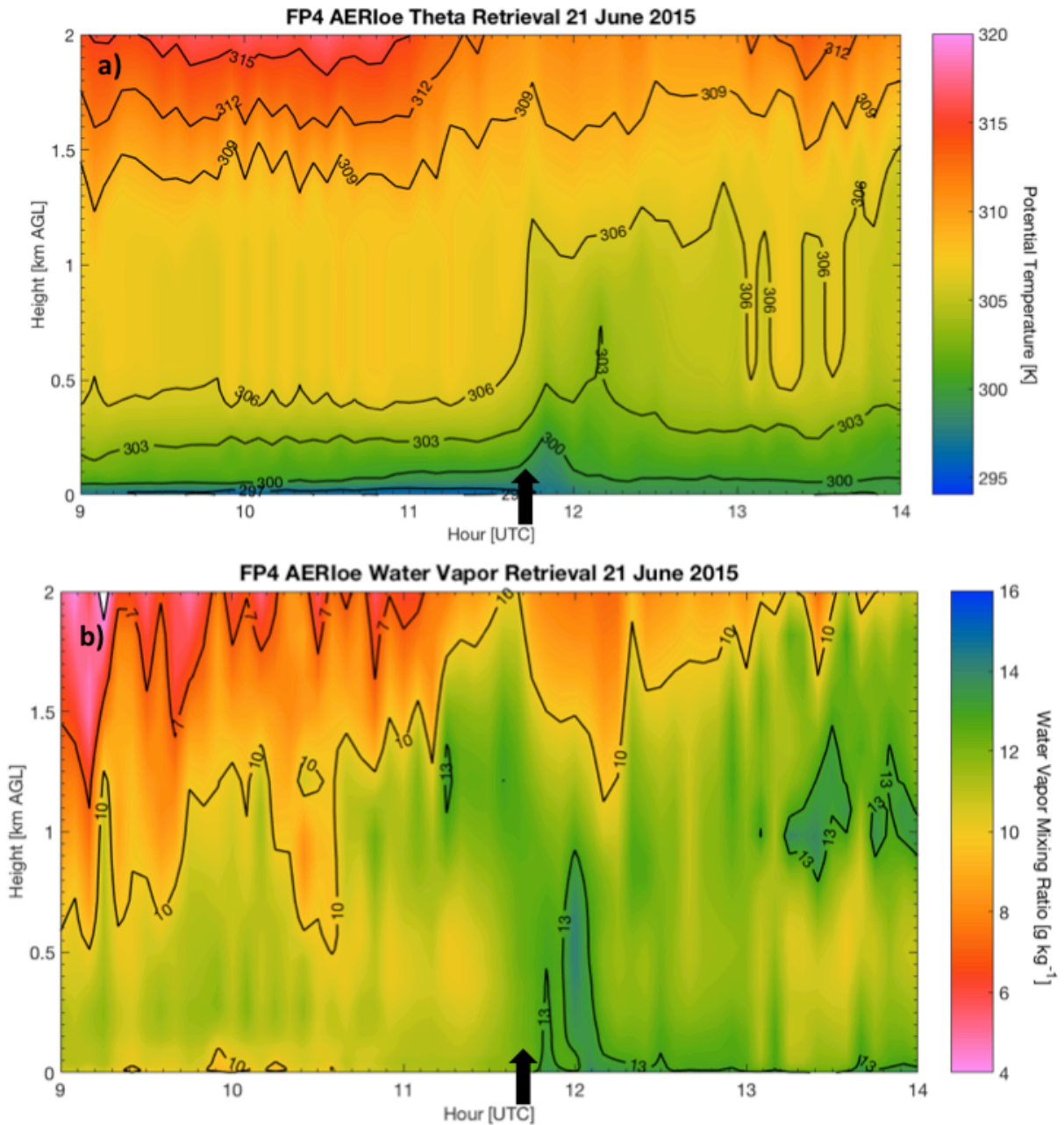
Figure 8.5: AERIoe retrieved a) potential temperature and b) water vapor mixing ratio time-height cross-section from FP4 in Minden, NE from 21 June 2015 from 0900 UTC to 1400 UTC. Potential temperature and water vapor mixing ratio is shaded, with isentropes and isohumes outlined and labeled every 3 K and 3 g kg^{-1}. The bore start time is 1150 UTC, denoted by the black arrows.
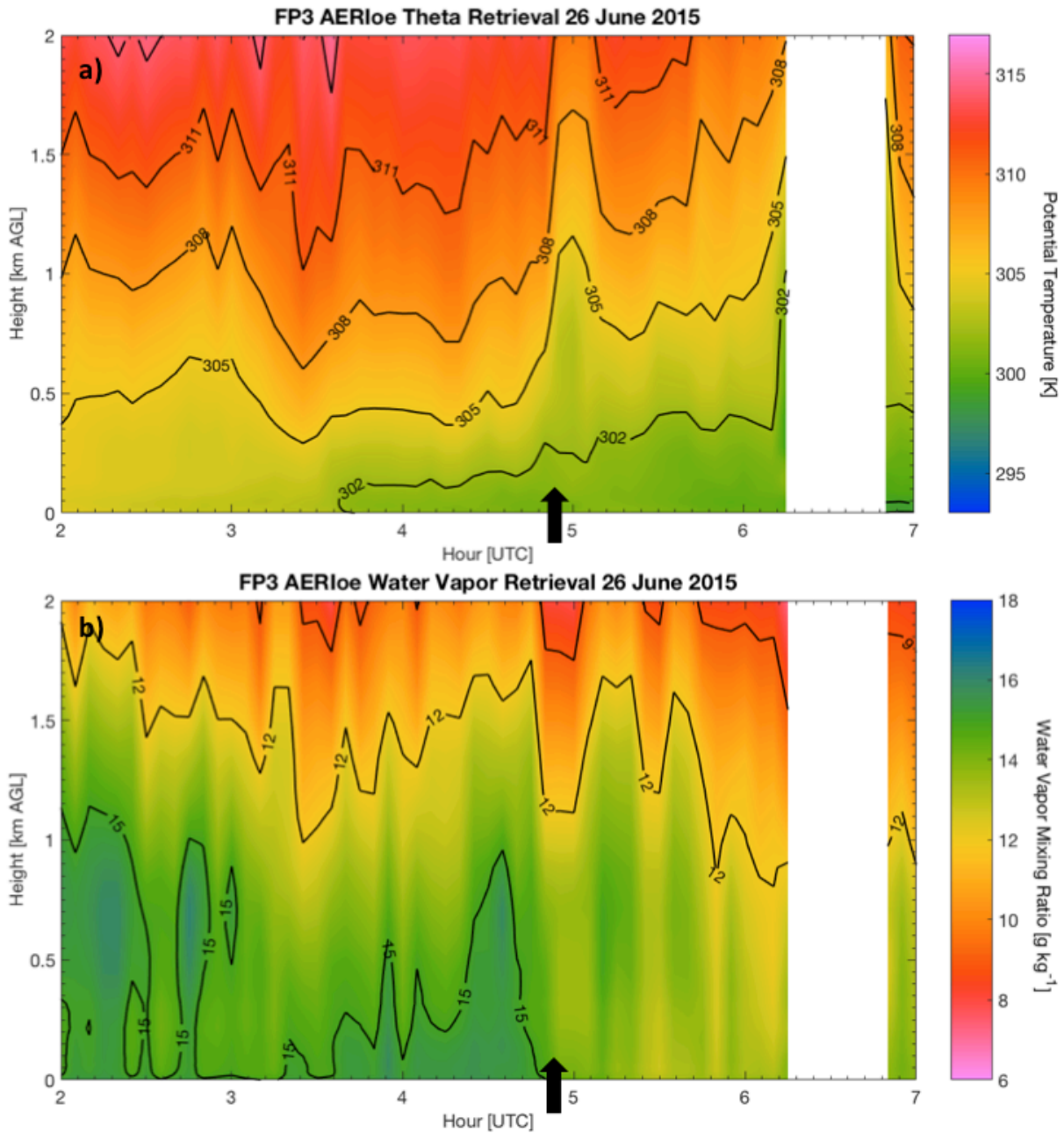
Figure 8.6: AERIoe retrieved a) potential temperature and b) water vapor mixing ratio time-height cross-section from FP3 in Ellis, KS from 26 June 2015 from 0200 UTC to 0700 UTC. Potential temperature and water vapor mixing ratio is shaded, with isentropes and isohumes outlined and labeled every 3 K and 3 g kg^{-1}. The bore start time is 0455 UTC, denoted by the black arrows. There are no retrievals between 0615 and 0650 UTC due to rain.

IX. Summary and Conclusions

This study developed a method to create a composite mean of 20 different bore events observed by AERIs during the PECAN campaign. Using this composite mean, the average character of a bore passage is analyzed. High-temporal resolution thermodynamic sounding retrievals from the AERIoe algorithm allow for the monitoring of the evolution of severe indices with the bore passage to assess the impact of the bore on potential convective initiation after passage. Two short case studies were conducted to assess the extremes in variability in overall CAPE trends among the 20 cases used in the study.

No other studies in the literature combine multiple bores with uniform instrumentation within a single methodology. Previous observational studies focused on one or two bores on the same day in the same area in the context of a case study. This combination of many bores into a single composite average allows for the general boundary layer trends of bores to be documented, along with their implications for convective initiation. This knowledge is presently lacking in the literature, as case studies of bores are likely picked due to their convective initiation potential; null convection cases are rarely investigated with the same depth. This study fills that gap in the literature and provides a general overview of typical conditions with bore passages, and makes progress at categorizing the variability of some of the changes that can occur with bore passages.

Key findings can be summarized as follows:

- The compositing method was proven to be useful to create a composite mean of pressure, temperature, water vapor mixing ratio, and wind variables and recreate a bore-like structure in time series of those atmospheric variables.

- A composite mean time series of convective indices was developed, which identified reductions in CIN and LFC height with the bore passage. This would favor future convective initiation behind the bore.

- Changes in CAPE were found to be highly variable, with the majority of cases resulting in decreased CAPE behind the bore, something that has not been frequently documented in previous case studies.

- The comparison of the two case studies provides evidence for active phase and dissipation stage bores to have differing influences on the potential for convective initiation. This result suggests that better understanding the differences between the two stages/phases should be a topic of further research.

Bores have been found to frequently result in decreases in CIN and LFC height. Another boundary trailing the bore could provide enough lift, given the bore's modification to the LFC height, to initiate convection, as was the case in Koch and Clark (1999). The lower CIN and LFC height would increase the potential for convective initiation, but the decrease in CAPE would reduce the severity of convection that may form in the post-bore environment. This is an important finding because without a nation-wide network of thermodynamic profilers in place or more frequent radiosonde launches from operational sites, the only method of identifying bores is using National Weather Service Doppler Radars (WSR-88Ds). Thus, the boundary layer transitions occurring with the bore passage are difficult to know; surface observations can only provide limited insight. While each individual bore seems to have a unique set of transitions associated with it, the results presented here provide forecasters with a general idea of what trends they can expect when they observe bores on radar. The average vertical parcel displacement as shown in the

composite was approximately 700 m. These results have important implications that can be applied to real-time forecasting of potential convective initiation, even given that operational forecasters have minimal knowledge of the bore.

Future work could include compositing bores based on active phase versus dissipation stages of their life cycles and the impacts on convection that follow from those changes if an objective way of discriminating between those bore types using typical instrumentation can be determined. The short case studies of the 21 June and 26 June bores at FP4 and FP3 presented in section 8 revealed the potential importance of active phase and dissipation stage bores, identified by Koch et al. (2008). The rapid drying of the boundary layer could potentially be a major source of stabilization behind active phase bores, while dissipation stage bores and their lofting of moisture could result in further destabilization of the boundary layer. Koch et al. (2008) identified the differences between the two bores based on their turbulent kinetic energy (TKE), which was modeled. TKE is difficult to observe with the instruments deployed at the various facilities during PECAN, and an obvious differentiation between the two bore types cannot be made to create a composite analysis focused on this difference. Furthermore, the drying and moistening of the boundary layer is only evidence of the differences in mixing between bore types, but it is dependent on the assumption of a sufficiently dry free troposphere, which is not always the case. The more vigorous mixing associated with active phase bores is also a result of stronger updrafts, which can make direct convective initiation by the bore more likely. Given the results of this study, it may be worthwhile for future work on the problem of bores and convective initiation to further investigate the differences between these two types of bores and their potential different implications for convective initiation.

References

Ashley, S. T., and W. S. Ashley, 2008: Flood fatalities in the United States. *J. Appl. Meteor. Climatol.*, **47**, 805-818.

Benjamin, S. G., and Coauthors, 2016: A North American hourly assimilation and model forecast cycle: The Rapid Refresh. *Mon. Wea. Rev.*, **144**, 1669-1694.

Blumberg, W. G., K. Halbert, T. Supinie, P. Marsh, R. Thompson, and J. Hart, 2017: SHARPpy: An open source sounding analysis toolkit for the atmospheric sciences. *Bull. Amer. Meteor. Soc.*, doi:10.1175/BAMS-D-15-00309.1, in press.

Christie, D. R., 1989: Long nonlinear waves in the lower atmosphere. *J. Atmos. Sci.*, **46**, 1462-1491.

Clarke, R. H, R. K. Smith, and D. G. Reid, 1981: The Morning Glory of the Gulf of Carpentaria: an atmospheric undular bore. *Mon. Wea. Rev.*, **109**, 1726-1750.

Coleman, T. A., K. R. Knupp, and D. E. Herzmann, 2010: An undular bore and gravity waves illustrated by dramatic time-lapse photography. *J. Atmos. Oceanic Technol.*, **27** 1355-1361.

____, and K. R. Knupp, 2011: Radiometer and profiler analysis of the effects of a bore and a solitary wave on the stability of the nocturnal boundary layer. *Mon. Wea. Rev.*, **139**, 211-223.

Colman, B. R., 1990: Thunderstorms above frontal surfaces in environments without positive CAPE. Part I: A climatology. *Mon. Wea. Rev.*, **118**, 1103-1121.

Crook, N. A. 1988: Trapping of low-level internal gravity waves. *J. Atmos. Sci.*, **45**, 1533-1541.

Davis, C. A., and Coauthors, 2004: The Bow Echo and MCV Experiment: observations and opportunities. *Bull. Amer. Meteor. Soc.*, **85**, 1075-1093.

Droegemeier, K. K., and R. B. Wilhelmson, 1987: Numerical simulation of thunderstorm outflow dynamics. Part I: Outflow sensitivity experiments and turbulence dynamics. *J. Atmos. Sci.*, **44**, 1180-1210.

Ecklund, W. L., D. A. Carter, B. B. Balsley, P. E. Currier, J. L. Green, B. L. Weber, and K. S. Gage, 1990: Field tests of a lower tropospheric wind profiler. *Radio Sci.*, **25**, 899-906.

Feltz, W. F., W. L. Smith, R. O. Knuteson, H. E. Revercomb, H. M. Woolf, and H. B. Howell, 1998: Meteorological applications of temperature and water vapor retrievals

from the ground-based atmospheric emitted radiance interferometer (AERI). *J. Appl. Meteor.*, **37**, 857-875.

____, and J. R. Mecikalski, 2002: Monitoring high-temporal resolution convective stability indices using the ground-based atmospheric emitted radiance interferometer (AERI) during the 3 May 1999 Oklahoma-Kansas tornado outbreak. *Wea. Forecasting*, **17**, 445-455.

____, W. L. Smith, H. B. Howell, R. O. Knuteson, H. Woolf, and H. E. Revercomb, 2003: Near-continuous profiling of temperature, moisture, and atmospheric stability using the atmospheric emitted radiance interferometer (AERI). *J. Appl. Meteor.*, **42**, 584-597.

Fritsch, J. M., R. J. Kane, and C. R. Chelius, 1986: The contribution of mesoscale convective weather systems to the warm-season precipitation in the United States. *J. Clim. Appl. Meteor.*, **25**, 1333-1345.

Geerts, B., and Coauthors, 2017: The 2015 Plains Elevated Convection At Night (PECAN) field project. *Bull. Amer. Meteor. Soc.*, **98**, 767-786.

Haase, S. P., and R. K. Smith, 1989: The numerical simulation of atmospheric gravity currents. Part II: Environments with stable layers. *Geophys. Astrophys. Fluid Dyn.*, **46**, 35-51.

Hartung, D. C., J. A. Otkin, J. E. Martin, D. D. Turner, 2010: The life cycle of an undular bore and its interaction with a shallow, intense cold front. *Mon. Wea. Rev.*, **138**, 886-908.

Heideman, K. F. and J. M. Fritsch, 1988: Forcing mechanism and other characteristics of significant summertime precipitation. *Wea. Forecasting*, **3**, 115-130.

Houze, R. A., 2004: Mesoscale convective systems. *Rev. Geophys.*, **42**, 1-43.

International Met Systems, 2006: iMet-1-ABxn Radiosonde. International Met Systems, 1 pp. [Available online at: http://intermetsystems.com/ee/pdf/202060_iMet-1-ABxn _Data_161006.pdf].

Karyampudi, V. M., S. E. Koch, C. Chen, J. W. Rottman, 1995: The influence of the Rocky Mountains on the 13 – 14 April 1986 severe weather outbreak. Part II: Evolution of a prefrontal bore and its role in triggering a squall line. *Mon. Wea. Rev.*, **123**, 1423-1446.

Knupp, K. R., 2006: Observational analysis of a gust front to bore to solitary wave transition within an evolving nocturnal boundary layer. *J. Atmos. Sci.*, **63**, 2016-2035.

Knuteson, R. O., and Coauthors, 2004a: Atmospheric emitted radiance interferometer (AERI). Part I: Instrument design. *J. Atmos. Oceanic Technol.*, **21**, 1763-1776.

____, and Coauthors, 2004b: Atmospheric emitted radiance interferometer (AERI). Part II: Instrument performance. *J. Atmos. Oceanic Technol.*, **21**, 1777-1789.

Koch, S. E., P. B. Dorian, R. Ferrare, S. H. Melfi, W. C. Skillman, and D. Whiteman, 1991: Structure of an internal bore and dissipating gravity current as revealed by Raman lidar. *Mon. Wea. Rev.*, **119**, 857-887.

____, and W. L. Clark, 1999: A nonclassical cold front observed during COPS-91: Frontal structure and the process of severe storm initiation. *J. Atmos. Sci.*, **56**, 2862-2890.

____, W. F. Feltz, F. Fabry, M. Pagowski, B. Geerts, K. M. Bedka, D. O. Miller, and J. W. Wilson, 2008: Turbulent mixing processes in atmospheric bores and solitary waves deduced from profiling systems and numerical simulation. *Mon. Wea. Rev.*, **136**, 1373-1400.

Lindseth, B., W. O. J. Brown, J. Jordan, D. Law, T. Hock, S. A. Cohn, and Z. Popović, 2012: A new portable 449-MHz spaced antenna wind profiler radar. *IEEE Trans. Geosci. Remote Sens.*, **50**, 3544-3553.

Locatelli, J. D., M. T. Stoelinga, P. V. Hobbs, and J. Johnson, 1998: Structure and evolution of an undular bore on the High Plains and its effects on migrating birds. *Bull. Amer. Meteor. Soc.*, 79, 1043-1060.

____, ____, ____, 2002: A new look at the Super Outbreak of tornadoes on 3 – 4 April 1974. *Mon. Wea. Rev.*, **130**, 1633-1651.

Maddox, R. A., C. F. Chappell, and L. R. Hoxit, 1979: Synoptic and meso-α scale aspects of flash flood events. *Bull. Amer. Meteor. Soc.*, **60**, 115-123.

Mahapatra, P. R., R. J. Doviak, and D. S. Zrnic, 1991: Multisensor observation of an atmospheric undular bore. *Bull. Amer. Meteor. Soc.*, **72**, 1468-1480.

Morse, C. S., R. K. Goodrich, and L. B. Cornman, 2002: The NIMA method for improved moment estimation from Doppler spectra. *J. Atmos. Oceanic Technol.*, **19**, 274-295.

Parker, M. D., 2008: Response of simulated squall lines to low-level cooling. *J. Atmos. Sci.*, **65**, 1323-1341.

Pearson, G., F. Davies, and C. Collier, 2009: An analysis of the performance of the EFAM pulsed Doppler lidar for observing the boundary layer. *J. Atmos. Oceanic Technol.*, **26**, 240-250.

Pu, B. and R. E. Dickinson, 2014: Diurnal spatial variability of Great Plains summer precipitation related to the dynamics of the low-level jet. *J. Atmos. Sci.*, **71**, 1807-1817.

Raymond, D. J., and H. Jiang, 1990: A theory for long-lived mesoscale convective systems. *J. Atmos. Sci.*, **47**, 3067-3077.

Rodgers, C. D., 2000: *Inverse Methods for Atmospheric Sounding: Theory and Practice.* Series on Atmospheric, Oceanic and Planetary Physics, Vol. 2, World Scientific, 238 pp.

Rottman, J. W., and J. E. Simpson, 1989: The formation of internal bores in the atmosphere: A laboratory model. *Quart. J. Roy. Meteor. Soc.*, **108**, 941-963.

Simpson, J. E., 1982: Gravity currents in the laboratory, atmosphere, and ocean. *Ann. Rev. Fluid. Mech.*, **14**, 213-234.

Smith. R. K, N. Crook, and G. Roff, 1982: The Morning Glory: an extraordinary atmospheric undular bore. *Quart. J. Roy. Meteor. Soc.*, **108**, 937-956.

Smith, R. K., 1988: Travelling waves and bores in the lower atmosphere: The 'Morning Glory' and related phenomena. *Earth-Sci. Rev.*, **25**, 267-290.

Smith, W. L., W.F. Feltz, R. O. Knuteson, H. E. Revercomb, H. M. Woolf, and H. B. Howell, The retrieval of planetary boundary layer structure using ground-based infrared spectral radiance measurements. *J. Atmos. Oceanic Technol.*, **16**, 323-333.

Tanamachi, R. L., W. F. Feltz, and M. Xue, 2008: Observations and numerical simulation of upper boundary layer rapid drying and moistening events during the International H_2O Project (IHOP_2002). *Mon. Wea. Rev.*, **136**, 3106-3120.

Tepper, M., 1950: A proposed mechanism of squall lines: the pressure jump line. *J. Meteor.*, **7**, 21-29.

Tripoli, G. J. and W. R. Cotton, 1989a: Numerical study of an observed orogenic mesoscale convective system. Part I: Simulated genesis and comparison with observations. *Mon. Wea. Rev.*, **117**, 273-304.

____, and ____, 1989b: Numerical study of an observed orogenic mesoscale convective system. Part II: Analysis of governing dynamics. *Mon. Wea. Rev.*, **117**, 305-328.

Turner, D. D, W. F. Feltz, and R. A. Ferrare, 2000: Continuous water vapor profiles from operational ground-based active and passive remote sensors. *Bull. Amer. Meteor. Soc.*, **81**, 1301-1317.

____, R. O. Knuteson, H. E. Revercomb, C. Lo, and R. G. Dedecker, 2006: Noise reduction of Atmospheric Emitted Radiance Interferometer (AERI) observations using principal component analysis. *J. Atmos. Oceanic Technol.*, **23**, 1223-1238.

____, and U. Löhnert, 2014: Information content and uncertainties in thermodynamic profiles and liquid cloud properties retrieved from the ground-based atmospheric emitted radiance interferometer (AERI). *J. Appl. Meteor. and Climatol.*, **53**, 752-771.

Tuttle, J. D., and C. A. Davis, 2006: Corridors of warm season precipitation in the central United States. *Mon. Wea. Rev.*, **134**, 2297-2317.

Vaisala, 2013: Vaisala Radiosonde RS92-SGP. Vaisala, 2 pp. [Available online at: http://www.vaisala.com/Vaisala%20Documents/Brochures%20and%20Datasheets/RS92SGP-Datasheet-B210358EN-F-LOW.pdf].

____, 2016: Vaisala Radiosonde RS41-SGP. Vaisala, 2 pp. [Available online at: http://www.vaisala.com/Vaisala%20Documents/Brochures%20and%20Datasheets/WEA-MET-RS41SGP-Datasheet-B211444EN.pdf].

Wagner, T. J., W. F. Feltz, and S. A. Ackerman, 2008: The temporal evolution of convective indices in storm-producing environments. *Wea. Forecasting*, **23**, 786-794.

Wakimoto, R. M, and D. E. Kingsmill, 1995: Structure of an atmospheric undular bore generated from colliding boundaries during CAPE. *Mon. Wea. Rev.*, **123**, 1374-1393.

Wallace, J. M., 1975: Diurnal variations in precipitation and thunderstorm frequency over the conterminous United States. *Mon. Wea. Rev.*, **103**, 406-419.

Weckwerth, T. M., and Coauthors, 2004: An overview of the International H_2O Project (IHOP_2002) and some preliminary highlights. *Bull. Amer. Meteor. Soc.*, **85**, 253-277.

Weisman, M. L., and Coauthors, 2015: The Mesoscale Predictability Experiment (MPEX). *Bull. Amer. Meteor. Soc.*, **96**, 2127-2149.

Wilson, J. W., and R. D. Roberts, 2006: Summary of convective storm initiation and evolution during IHOP: Observational and modeling perspective. *Mon. Wea. Rev.*, **134**, 23-47.

Wood, I. R., and J. E. Simpson, 1984: Jumps in layered miscible fluids. *J. Fluid Mech.*, **140**, 329-342.